A&A, 682, A129 (2024)
https://doi.org/10.1051/0004-6361/202347472
© The Authors 2024

Astronomy & Astrophysics

The GAPS programme at TNG

XLIX. TOI-5398, the youngest compact multi-planet system composed of an inner sub-Neptune and an outer warm Saturn★,★★

G. Mantovan[1,2], L. Malavolta[1,2], S. Desidera[2], T. Zingales[1,2], L. Borsato[2], G. Piotto[1], A. Maggio[3], D. Locci[3], D. Polychroni[4], D. Turrini[5], M. Baratella[6], K. Biazzo[7], D. Nardiello[2], K. Stassun[8,9], V. Nascimbeni[2], S. Benatti[3], A. Anna John[10], C. Watkins[11], A. Bieryla[11], J. J. Lissauer[12], J. D. Twicken[13,14], A. F. Lanza[15], J. N. Winn[16], S. Messina[15], M. Montalto[15], A. Sozzetti[5], H. Boffin[17], D. Cheryasov[18], I. Strakhov[18], F. Murgas[19,20], M. D'Arpa[3], K. Barkaoui[21,22,19], P. Benni[23], A. Bignamini[4], A. S. Bonomo[5], F. Borsa[24], L. Cabona[2], A. C. Cameron[10], R. Claudi[2,38], W. Cochran[25], K. A. Collins[11], M. Damasso[5], J. Dong[26,★★★], M. Endl[25], A. Fukui[32,19], G. Fűrész[27], D. Gandolfi[40], A. Ghedina[28], J. Jenkins[14], P. Kabáth[29], D. W. Latham[11], V. Lorenzi[19,28], R. Luque[30], J. Maldonado[3], K. McLeod[31], M. Molinaro[4], N. Narita[19,32,33], G. Nowak[19,20,34], J. Orell-Miquel[19,20], E. Pallé[19,20], H. Parviainen[19,20], M. Pedani[28], S. N. Quinn[11], H. Relles[11], P. Rowden[35], G. Scandariato[15], R. Schwarz[11], S. Seager[27,36], A. Shporer[27], A. Vanderburg[39,★★★★], and T. G. Wilson[37]

(Affiliations can be found after the references)

Received 14 July 2023 / Accepted 25 October 2023

ABSTRACT

Context. Short-period giant planets ($P \lesssim 10$ days, $M_p > 0.1\ M_J$) are frequently found to be solitary compared to other classes of exoplanets. Small inner companions to giant planets with $P \lesssim 15$ days are known only in five compact systems: WASP-47, Kepler-730, WASP-132, TOI-1130, and TOI-2000. Here, we report the confirmation of TOI-5398, the youngest known compact multi-planet system composed of a hot sub-Neptune (TOI-5398 c, $P_c = 4.77271$ days) orbiting interior to a short-period Saturn (TOI-5398 b, $P_b = 10.590547$ days) planet, both transiting around a 650 ± 150 Myr G-type star.

Aims. As part of the Global Architecture of Planetary Systems (GAPS) Young Object project, we confirmed and characterised this compact system, measuring the radius and mass of both planets, thus constraining their bulk composition.

Methods. Using multi-dimensional Gaussian processes, we simultaneously modelled stellar activity and planetary signals from the Transiting Exoplanet Survey Satellite (TESS) Sector 48 light curve and our High Accuracy Radial velocity Planet Searcher (HARPS-N) radial velocity (RV) time series. We confirmed the planetary nature of both planets, TOI-5398 b and TOI-5398 c, and obtained a precise estimation of their stellar parameters.

Results. Through the use of astrometric, photometric, and spectroscopic observations, our findings indicate that TOI-5398 is a young, active G dwarf star (650 ± 150 Myr) with a rotational period of $P_{rot} = 7.34$ days. The transit photometry and RV measurements enabled us to measure both the radius and mass of planets b, $R_b = 10.30 \pm 0.40\ R_\oplus$, $M_b = 58.7 \pm 5.7\ M_\oplus$, and c, $R_c = 3.52 \pm 0.19\ R_\oplus$, $M_c = 11.8 \pm 4.8\ M_\oplus$. TESS observed TOI-5398 during sector 48 and no further observations are planned in the current Extended Mission, making our ground-based light curves crucial for improvement of the ephemeris. With a transmission spectroscopy metric (TSM) value of around 300, TOI-5398 b is the most amenable warm giant ($10 < P < 100$ days) for JWST atmospheric characterisation.

Key words. planetary systems – planets and satellites: fundamental parameters – stars: fundamental parameters – stars: individual: BD+37 2118 – techniques: photometric – techniques: radial velocities – planet-star interactions

1. Introduction

Multi-planet systems provide a unique opportunity to investigate comparative planetary science and understand the interactions and processes between their planets (e.g. Dragomir et al. 2019; Kostov et al. 2019; Lacedelli et al. 2021; Trifonov et al. 2023). By studying the relative planet sizes and orbital separations, the obliquity between the planetary orbital planes and the stellar rotation axis, and other parameters, we can constrain the formation and evolution processes of these systems (see, e.g. Mancini et al. 2022; Grouffal et al. 2022). The precise measurement of the orbital architecture and the bulk composition of the planets is essential in order to fully characterise similar systems. In this context, high-precision radial velocities (RVs) are necessary in order to derive masses and eccentricities, which, combined with the radii from transit, allow us to measure precise inner

★ Table A.1 is available at the CDS ftp to cdsarc.cds.unistra.fr (130.79.128.5) or via https://cdsarc.cds.unistra.fr/viz-bin/cat/J/A+A/682/A129

★★ Based on observations made with the Italian Telescopio Nazionale *Galileo* (TNG) operated by the Fundación Galileo Galilei (FGG) of the Istituto Nazionale di Astrofisica (INAF) at the Observatorio del Roque de los Muchachos (La Palma, Canary Islands, Spain).

★★★ Flatiron Research Fellow.

★★★★ NASA Sagan Fellow.

Open Access article, published by EDP Sciences, under the terms of the Creative Commons Attribution License (https://creativecommons.org/licenses/by/4.0), which permits unrestricted use, distribution, and reproduction in any medium, provided the original work is properly cited.
This article is published in open access under the Subscribe to Open model. Subscribe to A&A to support open access publication.

bulk densities and finally to explore the differences in planetary structure and evolution.

The architecture of multi-planet systems is highly diverse, with planets spanning the whole range of masses and grouped in a wide variety of dynamical configurations. However, short-period giant planets ($P \lesssim 10$ days) are typically isolated planets compared to other classes of exoplanets (Huang et al. 2016), and their companions, if present, are often massive long-period planets with $P > 200$ days (Knutson et al. 2014; Schlaufman & Winn 2016). Compactness is a rare feature among known multi-planet systems with inner giant planets. Moreover, there is a scarcity of known compact systems composed of a close-orbit outer jovian-size planet and an inner orbit small-size planet (e.g. Hord et al. 2022). This family of unique planetary systems is presently composed of WASP-47 (Hellier et al. 2012), Kepler-730 (Zhu et al. 2018; Cañas et al. 2019), TOI-1130 (Huang et al. 2020a; Korth et al. 2023), TOI-2000 (Sha et al. 2023), and WASP-132 (Hord et al. 2022).

Studying planets younger than 1 Gyr is crucial for understanding the mechanisms at play during the early stages of planetary formation and evolution, such as orbital migration, atmospheric evaporation, planetary impacts, and so on (see e.g. Terquem & Papaloizou 2007; Bonomo et al. 2019). However, it is challenging to identify and model such systems, because of the magnetic activity of the host star. Indeed, both the photometric and spectroscopic time series are affected by the variations in star flux caused by the numerous star spots, faculae, the faculae network, and the strong magnetic activity on the stellar surface. Despite the stellar activity that hides planetary signals, researchers have discovered planets orbiting members of young stellar clusters (Malavolta et al. 2016; Newton et al. 2019; Mann et al. 2020; Bouma et al. 2020), young stellar associations and moving groups (Benatti et al. 2019; Damasso et al. 2023), and even young field stars (Desidera et al. 2023). There is an increasing number of young exoplanets with well-constrained ages, radii, and masses. Within the Global Architecture of Planetary Systems (GAPS, Covino et al. 2013; Carleo et al. 2020) Young Objects (YO) long-term program at Telescopio Nazionale *Galileo* (TNG), many systems with young transiting planets first identified by space missions such as *Kepler* (Borucki et al. 2010), K2 (Howell et al. 2014), and TESS (Transiting Exoplanet Survey Satellite, Ricker et al. 2015) are being characterised through intense RV monitoring (e.g. Carleo et al. 2021; Nardiello et al. 2022).

Among the systems under intensive scrutiny by GAPS, the moderately young (~650 Myr) solar-analogue star TOI-5398 (BD+37 2118) is of special interest. In this paper, we characterise the compact multi-planet system orbiting this star using a combination of TESS and ground-based photometry, and RVs collected with the High Accuracy Radial velocity Planet Searcher (HARPS-N, Cosentino et al. 2012) spectrograph (Sect. 2). The TESS pipeline identified two candidate exoplanets: a transiting sub-Neptune (TOI-5398.02, $P \sim 4.77$ d) and a giant planet ($P \sim 10.59$ d) that has been thoroughly validated by Mantovan et al. (2022) and labelled TOI-5398 b. In Sect. 3, we report the stellar properties determined using two independent methods. Section 4 reports the procedures used to identify and confirm the two planets in the system by outlining the detailed modelling of photometry and RV. In Sect. 5, we discuss our results, provide suggestions for follow-up observations, highlight the rarity of our system, and call attention to the exquisite suitability of TOI-5398 b for future atmospheric characterisation. Concluding remarks are provided in Sect. 6.

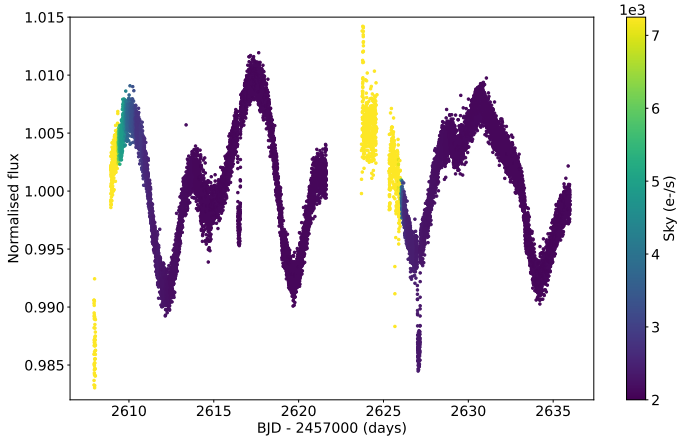

Fig. 1. SAP-corrected light curve of TOI-5398, observed in Sector 48. The local background value is colour-coded. Yellow points – with local background values >4σ above its mean value along the light curve – have been excluded from all analyses.

2. Observations

2.1. TESS photometry

The TESS mission observed TOI-5398 (TIC 8260536) at 2 min cadence in Sector 48 from 2022 January 28 to 2022 February 26. In particular, we considered the TESS Science Processing Operations Center (SPOC; Jenkins et al. 2016) Simple Aperture Photometry (SAP; Twicken et al. 2010; Morris et al. 2020) flux light curve and corrected it for time-correlated instrumental signatures. We corrected the light curve using Cotrending Basis Vectors (CBVs) extracted through the algorithm by Nardiello et al. (2020) as well as all SAP light curves in the same Camera and CCD as TOI-5398. We did this rather than using the Presearch Data Conditioning Simple Aperture Photometry (PDCSAP) light curve from the SPOC because, with the latter, the target experienced numerous systematic effects (Smith et al. 2012; Stumpe et al. 2012, 2014) as a result of over-corrections and/or injection of spurious signals.

In this study, we used light-curve points flagged with cadence quality flag values equal to 0 and associated with local background values <4σ above its mean[1] value along the light curve. The only exceptions to this rule are the points before BTJD[2] = 2609, which are flagged with a quality flag value equal to 32 768[3] and had local background values of up to 7σ above the mean. We did this to preserve one of the four genuine transits of TOI-5398.02. The corrected light curve shown in Fig. 1 displays a clear modulation that we attribute to stellar rotation. Therefore, to identify a rotation period of TOI-5398, we computed the generalised Lomb-Scargle (GLS) periodogram (Zechmeister & Kürster 2009) of the aforementioned light curve. The periodogram reveals the most powerful peak at 7.18 ± 0.21 days; see Fig. 2. The link between this peak and the rotational period of the star is discussed in Sect. 3.5. The light curve also exhibits two clear dips at BTJD ~ 2616 and 2627, which were shown by Mantovan et al. (2022) to be caused by a substellar companion.

[1] Mean of the sigma-clipped data, computed using `Astropy`.
[2] BTJD = $\mathrm{BJD_{TDB}} - 2\,457\,000.0$.
[3] "Insufficient Targets for Error Correction Exclude" https://outerspace.stsci.edu/display/TESS/2.0+-+Data+Product+Overview

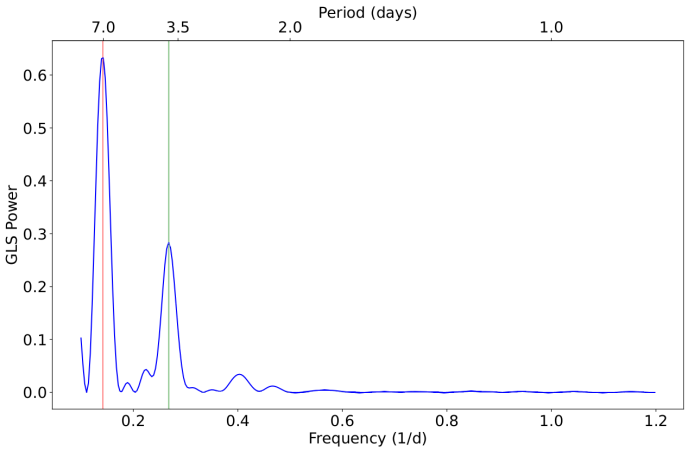

Fig. 2. GLS periodogram of the TESS SAP photometry corrected for time-correlated instrumental signatures. The vertical lines indicate the period at 7.18 days and its first harmonic.

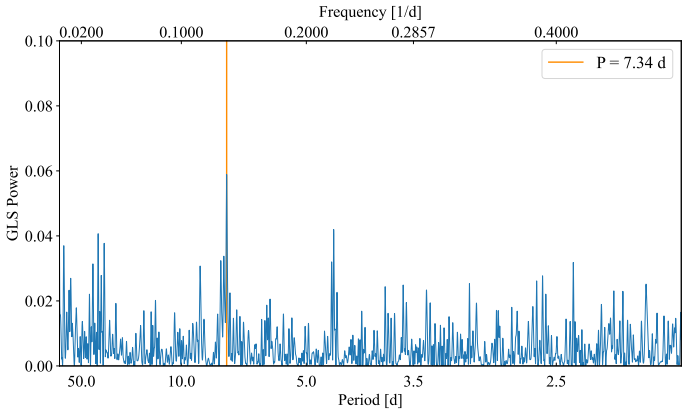

Fig. 3. GLS periodogram of the ASAS-SN photometry. The vertical line indicates the stellar rotation period at 7.34 days.

2.2. ASAS-SN

We downloaded almost 3 yr of archival data from ASAS-SN (Shappee et al. 2014; Kochanek et al. 2017), spanning from October 2020 to May 2023. The ASAS-SN images have a resolution of 8 arcsec pixel^{-1} ($\sim$15″ FWHM PSF), and the observations of TOI-5398 were conducted in the Sloan g−band. We checked the light curve to further constrain the stellar rotation period identified from the TESS photometry. We extracted the GLS periodogram, which reveals the most powerful peak with a period of 7.34 ± 0.01 days; see Fig. 3.

2.3. Photometric follow-up (TASTE)

A partial transit of TOI-5398 b was observed on 2023 January 31 by The Asiago Search for Transit timing variations of Exoplanets (TASTE) programme, a long-term campaign to monitor transiting planets (Nascimbeni et al. 2011). To prevent saturation and increase the photometric accuracy, the Asiago Faint Objects Spectrograph and Camera (AFOSC) camera, mounted on the *Copernico* 1.82-m telescope at the Asiago Astrophysical Observatory in northern Italy, was purposely defocused up to 8″ FWHM. A Sloan r' filter was used to acquire 2916 frames with a constant exposure time of 5 s. A preselected set of suitable reference stars was always imaged in the same field of view in order to apply precise differential photometry. At the end of the series, the sky transparency was highly variable, and thick clouds passed by during the off-transit, leaving us with a subset of 2721 images with a good signal-to-noise ratio (S/N).

We reduced the Asiago data with the STARSKY code (Nascimbeni et al. 2013), a software pipeline specifically designed to perform differential photometry on defocused images. After a standard correction through bias and flat-field frames, the size of the circular apertures and the weights assigned to each reference star were automatically chosen by the code to minimise the photometric scatter of our target. The time stamps were consistently converted to the $\mathrm{BJD_{TDB}}$ standard following Eastman et al. (2010), as done for the following photometric data sets as well.

2.4. Photometric follow-up (TFOP)

The TESS pixel scale is $\sim$21″/pixel and photometric apertures typically extend out to roughly 1 arcmin, generally causing multiple stars to blend in the TESS aperture. To determine the true source of transit signals in the TESS data, improve the transit ephemerides, monitor for transit timing variations, and check the SPOC pipeline transit depth after accounting for the crowding metric, we conducted ground-based light-curve follow-up observations of the field around TOI-5398 as part of the TESS Follow-up Observing Program[4] Sub Group 1 (TFOP; Collins 2019). We used the `TESS Transit Finder`, which is a customised version of the `Tapir` software package (Jensen 2013), to schedule our transit observations. All the image data were calibrated, and all photometric data were extracted using `AstroImageJ` unless stated otherwise. We used circular photometric apertures centred on TOI-5398, and also checked the flux from the nearest known neighbour in the *Gaia* DR3 (Gaia Collaboration 2023) and TICv8 catalogues (TIC 8260534), which is $\sim$37″ northeast of TOI-5398.

2.4.1. LCOGT

We observed four and two partial transit windows of TOI-5398 b and TOI-5398.02, respectively, in Pan-STARRS z-short band using the Las Cumbres Observatory Global Telescope (LCOGT; Brown et al. 2013) 1.0 m network nodes at Teide Observatory (TEID) on the island of Tenerife, McDonald Observatory (MCD) near Fort Davis, Texas, United States, and Cerro Tololo Inter-American Observatory in Chile (CTIO). We observed an ingress and egress of TOI-5398 b on UTC 2022 April 21 from TEID and MCD, respectively, an egress on UTC 2023 March 4 from TEID, and an ingress on UTC 2023 March 15 from MCD. We observed an egress of TOI-5398.02 on UTC 2022 April 2 from CTIO, and an ingress on UTC 2022 May 10 from MCD. The 1 m telescopes are equipped with 4096×4096 Sinistro cameras with an image scale of 0.389″/pixel, resulting in a $26' \times 26'$ field of view. The images were calibrated using the standard LCOGT `BANZAI` pipeline (McCully et al. 2018). We used circular photometric apertures with radii in the range of 5.1″ to 7.4″, which excluded all of the flux from TIC 8260534.

2.4.2. Acton Sky Portal

A full transit window of TOI-5398 b was observed in Sloan i' band on UTC 2022 April 21 from the Acton Sky Portal private observatory in Acton, MA, USA. The 0.36 m telescope is

[4] https://tess.mit.edu/followup

equipped with a SBIG Alumna CCD4710 camera with an image scale of 1.0 arcsec/pixel, resulting in a 17.1 × 17.1 arcmin field of view. We used a circular photometric aperture with a radius of 9″, which excluded all of the flux from TIC 8260534.

2.4.3. Whitin

A full transit window of TOI-5398 b was observed in Sloan r' band on UTC 2022 April 21 using the Whitin observatory 0.7 m telescope in Wellesley, MA, USA. The 2048 × 2048 FLI ProLine PL23042 detector has an image scale of 0.68″ pixel^{-1}, resulting in a 23.2 × 23.2 arcmin field of view. We used a circular photometric aperture with a radius of 8.2 arcsec, which excluded all of the flux from TIC 8260534.

2.4.4. KeplerCam

We obtained photometric observations using the KeplerCam CCD on the 1.2 m telescope at the Fred Lawrence Whipple Observatory (FLWO) at Mount Hopkins, Arizona, to observe an egress of TOI-5398 b. Observations were taken in the Sloan z' band on UT 2022 April 21. KeplerCam is a 4096 × 4096 Fairchild detector with a field of view of 23′x23′ and an image scale of 0.672″ pixel^{-1} when binned by 2. We used circular photometric apertures with radius 6.7″, which excluded all of the flux from TIC 8260534.

2.4.5. MuSCAT2

TOI-5398 was observed by MuSCAT2 on the night of 2022 March 30. MuSCAT2 is a multi-band imager (Narita et al. 2019) mounted on the Telescopio Carlos Sánchez (TCS, 1.52 m) at Teide Observatory, Spain. The instrument is capable of obtaining simultaneous images in Sloan g', r', i', and z_s bands with little readout time. Each camera has a field of view of 7.4′ × 7.4′ and a pixel scale of 0.44″/pixel.

The observation was made with the telescope defocused to avoid the saturation of the target. On the night of 2022 March 30, the i'-band camera presented technical issues and could not be used; the exposure times were set to 10, 5, and 10 s in g', r', and z_s, respectively. Standard data reduction, aperture photometry, and a transit model fit including systematic noise were carried out using the MuSCAT2 pipeline (Parviainen 2015; Parviainen et al. 2019).

2.4.6. Results

Due to their low S/N and to reduce the computational cost, we decided not to include light curves observed with LCOGT-CTIO and Whitin in our analysis. All other observations resulted in clear transit detections and the light-curve data are included in the joint modelling in Sect. 4.2 of this work.

2.5. HARPS-N spectroscopic follow-up

We collected observations of TOI-5398 with HARPS-N at TNG spanning the period between May 2022 and June 2023 and obtained a total of 86 spectra, with exposure times ranging from 900 to 1200 s. These spectra cover the wavelength range 383–693 nm with a resolving power of $R \sim 115\,000$. We performed the observations within the framework of the GAPS project and incorporated 10 h coming from a time-sharing agreement (proposal A46TAC_32, PI: G. Mantovan). Additionally, we included eight off-transit spectra from the DDT proposal A46DDT4 (PI: G. Mantovan) in our analysis, which we binned from 600 to 1200 s of exposure time. Six spectra taken in Spanish time (CAT22A_48, PI: E. Pallé) are also included in a comprehensive analysis of the object. We excluded from our final analysis one of these six spectra as it was collected during the in-transit phase of planet b. We decided to proceed in this way after considering the expected amplitude of the Rossiter-McLaughlin (Ohta et al. 2005) signature, which is further discussed in Sect. 5.4. We report the details about the observations and typical S/N in Table 1.

Table 1. Observations from TESS and HARPS-N summarised.

TOI-5398		
Dataset	Parameter	Value
TESS	Sector	48
	Camera	1
	CCD	1
HARPS-N	N° spectra	86
	Time-span (days)	439
	$\sigma_{\rm RV}$ (m s^{-1})	29
	$\langle {\rm RV_{err}} \rangle$ (m s^{-1})	3.5
	$\langle {\rm S/N} \rangle_{5460\,\text{Å}}$	64

We reduced the data collected using the HARPS-N Data Reduction Software (DRS 3.7.0), and we computed the RV through the cross-correlation function (CCF) method (Pepe et al. 2002 and references therein). With this method, the scientific spectra are cross-correlated with a binary mask describing the typical features of a star with a chosen spectral type. We used a G2 mask for TOI-5398. The resulting CCFs provide us with a representation of the mean line profile of each spectrum. However, the high levels of stellar activity might distort the core of the average line profile, and the stellar rotation broadens the line. Therefore, we needed to proceed with care in selecting the half-window for the evaluation of the CCF and use a width large enough to include the continuum when fitting the CCF profile (see Damasso et al. 2020). We decided to use the G2 mask with a half-window of 40 km s^{-1} (instead of the default value of 20 km s^{-1}) and reprocessed our data using the DRS version implemented through the YABI workflow interface (Hunter et al. 2012) at the Italian Center for Astronomical Archives[5]. We obtained RVs with a dispersion of a few tens of m s^{-1} (∼29 m s^{-1}), while their internal errors are approximately a few m s^{-1} (∼3.5 m s^{-1}).

To assess the jitter in the RV series caused by the stellar activity, we additionally extracted a set of activity indices. The value of the CCF bisector span (BIS), the full width at half-maximum (FWHM) depth of the CCF, and its equivalent width ($W_{\rm CCF}$, see Collier Cameron et al. 2019 for further details) are provided by the HARPS-N DRS, while the log R'_{HK} index from the Ca II H&K lines was obtained using a method available on YABI (based on the prescriptions of Lovis et al. 2011 and references therein) and using the $(B-V)_0$ colour index quoted in Sect. 3. Finally, we extracted the Hα index using the ACTIN 2 Code[6] (Gomes da Silva et al. 2018, 2021). Figure 4 displays the spectroscopic time series.

[5] https://www.ia2.inaf.it/
[6] https://github.com/gomesdasilva/ACTIN2

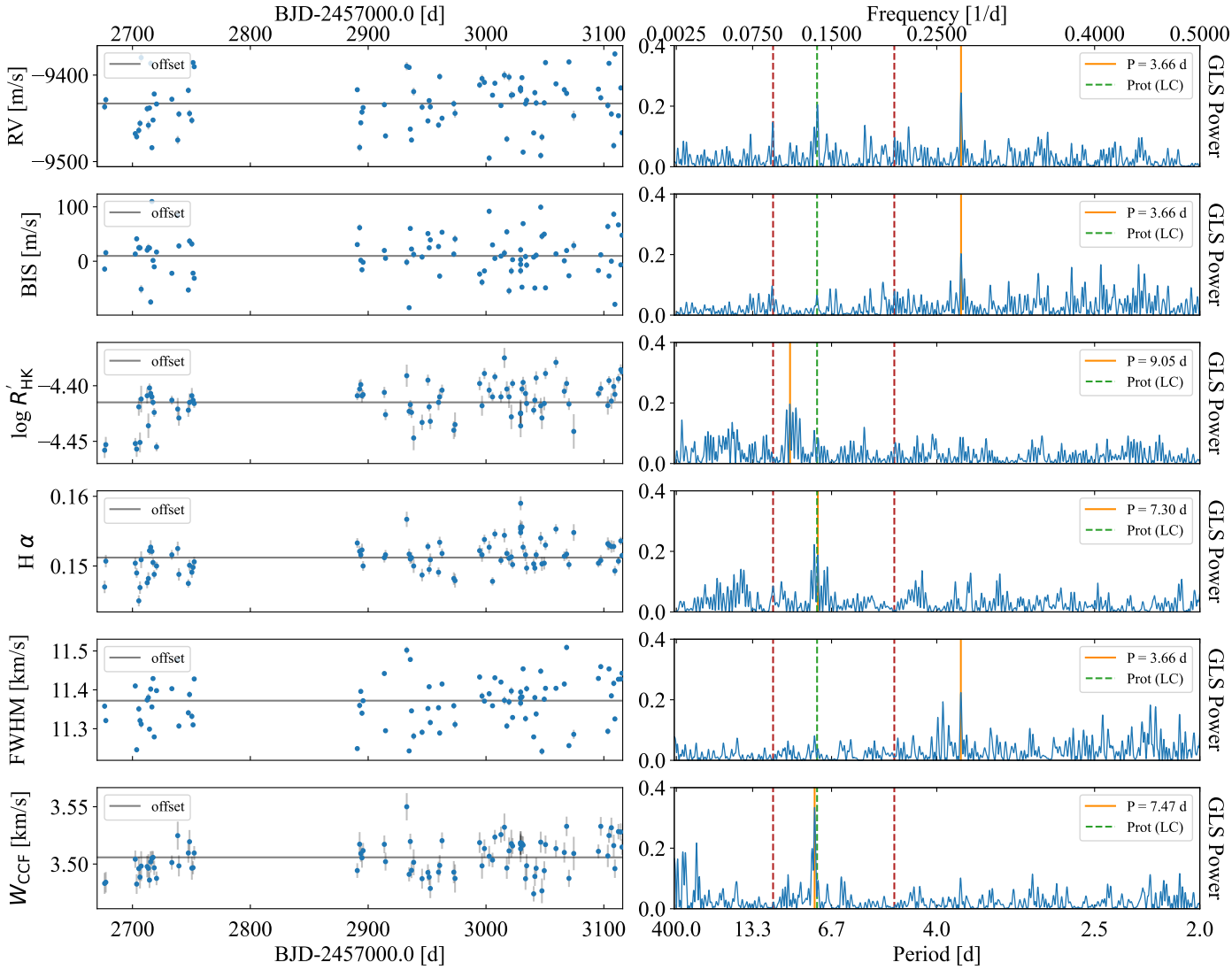

Fig. 4. Spectroscopic time series and GLS periodograms. *Left:* HARPS-N spectroscopic time series used in this work. The time series for RV, BIS, $\log R'_{HK}$, Hα, FWHM, and W_{CCF} are shown in the panels in order from top to bottom. *Right:* GLS periodogram of the RVs and the spectroscopic activity indicators under analysis. The primary peak of each periodogram is indicated by a vertical orange line. The dotted green lines represent the stellar rotation period described in Sect. 2.2. The signals along the red dotted vertical lines correspond to the transit-like signals with periods 4.77 and 10.59 d.

We also obtained moderately precise RVs with the Tull spectrograph at the Harlan J. Smith 2.7 m telescope at McDonald Observatory. These can be found in the Appendix.

2.6. High-angular-resolution data

TOI-5398 was also observed on 2022 December 2 with the speckle polarimeter on the 2.5 m telescope at the Caucasian Observatory of Sternberg Astronomical Institute (SAI) of Lomonosov Moscow State University. Speckle polarimeter uses the high-speed low-noise CMOS detector Hamamatsu ORCA–quest (Strakhov et al. 2023). The atmospheric dispersion compensator was active, which allowed us to use the I_c band. The respective angular resolution is 0.083″, while the long–exposure atmospheric seeing was 0.6″. We did not detect any stellar companions brighter than ΔI_c = 4.0 and 6.8 mag at ρ = 0.25″ and 1.0″, respectively, where ρ is the separation between the source and the potential companion (Fig. 5).

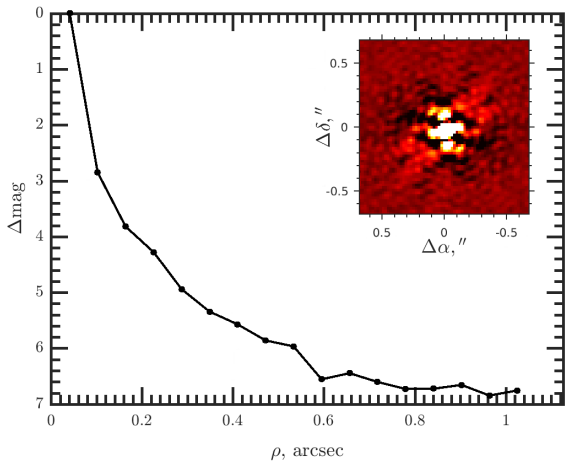

Fig. 5. High angular resolution speckle imaging of TOI- 5398 in I_c filter using the SAI 2.5 m telescope.

3. The host star

3.1. Atmospheric parameters and metallicity

Given the relatively young age of TOI-5398, we analysed the HARPS-N combined spectrum following the same methodology as, for example, in Nardiello et al. (2022) and Damasso et al. (2023). Specifically, we adopted an innovative approach to derive the stellar parameters with the equivalent width (EW) method using a combination of iron (Fe) and titanium (Ti) lines. In this way, we avoid issues related to the effect of the stellar activity that can shape the stellar spectrum at young ages (for a detailed explanation we refer the reader to Baratella et al. 2020a,b). Our initial guesses of the atmospheric parameters were estimated with *Gaia* DR3 (Gaia Collaboration 2016) and 2MASS photometry (Cutri et al. 2003) using the tool `colte` (Casagrande et al. 2021) and adopting $E(B-V) = 0.008 \pm 0.016$ (Lallement et al. 2014; Capitanio et al. 2017). The photometric estimates vary from 5978 ± 65 K in $(G_{\rm BP} - J)$ to 6039 ± 34 K in $(G_{\rm RP} - H)$. From these initial values and taking the *Gaia* parallax into account, we derived 4.44 ± 0.09 dex as input surface gravity, while an initial microturbulence $\xi = 1.07 \pm 0.05$ km s^{-1} was estimated from the relation by Dutra-Ferreira et al. (2016).

The final stellar parameters ($T_{\rm eff}$, $\log g$, ξ, [Fe/H]) were then derived through the MOOG code (Sneden 1973) and adopting the ATLAS9 grid of model atmospheres with new opacities (Castelli & Kurucz 2003). Our spectroscopic analysis provides final atmospheric parameters of $T_{\rm eff} = 6000 \pm 75$ K, $\log g = 4.44 \pm 0.10$ dex, and $\xi = 1.12 \pm 0.12$ km s^{-1}, which are in excellent agreement with the initial guesses. The derived iron abundance (computed with respect to the solar Fe abundance as in Baratella et al. 2020a) is [Fe/H]= $+0.09 \pm 0.06$, while the titanium abundance is [Ti/H]= $+0.08 \pm 0.05$, where the errors include the scatter due to the EW measurements and the uncertainties in the stellar parameters. Despite the error bars, there is an indication of a slightly super-solar metallicity.

3.2. Projected rotational velocity

With the same code and model atmospheres described in Sect. 3.1, we adopted the atmospheric parameters ($T_{\rm eff}$, $\log g$, ξ, [Fe/H]) previously derived to measure the stellar projected rotational velocity ($v \sin i_\star$). In particular, fixing the macroturbulence velocity to the value of 3.8 km s^{-1} from the relationship by Doyle et al. (2014), we applied the spectral synthesis method within MOOG for three spectral regions around 5400, 6200, and 6700 Å. Our final value of $v \sin i_\star$ is 7.5 ± 0.6 km s^{-1}. We refer readers to Biazzo et al. (2022) for the procedure based on spectral synthesis and the description of the uncertainty measurement.

3.3. Lithium abundance

As the lithium line at λ 6707.8 Å in the co-added spectrum of TOI-5398 was found to be blended with the iron line at λ 6707.4 Å, we applied the spectral synthesis technique, as in Sect. 3.2. Using MOOG and the Castelli & Kurucz (2003) model atmospheres, we fixed the stellar parameters and $v \sin i_\star$ to the values derived in the previous steps. Then, adopting two different line lists by Carlberg et al. (2012) and Chris Sneden (priv. comm.), and applying the non-LTE calculations of Lind et al. (2009), we obtained a lithium abundance of $\log n({\rm Li})_{\rm NLTE} = 2.82 \pm 0.11$, where the error bar considers uncertainties in the line list, in stellar parameters, and in the definition of the continuum position around the Li line. With its effective temperature and lithium abundance, the position of our target in the $\log n({\rm Li}) - T_{\rm eff}$ appears to be in between that of the M35 cluster (~200 Myr) and that of the Hyades cluster (~650 Myr; see e.g. Sestito & Randich 2005; Cummings et al. 2017).

3.4. Chromospheric activity

The lower chromosphere Ca II H&K emission was measured on HARPS-N spectra using YABI (see Sect. 2.5). The average value of the S-index calibrated in the Mt. Wilson scale (Baliunas et al. 1995) is 0.325, which corresponds to $\log R'_{\rm HK} = -4.43 \pm 0.02$ (arithmetic average and standard deviation).

For the $\log R'_{\rm HK}$ determination, we adopted $(B-V)_0 = 0.58$ mag, which was derived from $T_{\rm eff}$ using the Casagrande et al. (2006) calibration, as the observed values from *Tycho*2 and APASS suffer from large uncertainties. Our determination of $\log R'_{\rm HK}$ implies a stellar age of 370 Myr using the activity–age calibration and an expected rotation period of 4.25 d (corresponding to a gyrochronology age of 260 Myr) according to the relation presented by Mamajek & Hillenbrand (2008). The difference with the observed photometric period (see Sect. 3.5) is not significant considering the observational errors and the intrinsic scatter of magnetic activity (see e.g. Fig. 7 of Mamajek & Hillenbrand 2008). It is possible that the star is caught by chance at a higher-than-average level of chromospheric activity or that the activity is somewhat enhanced by the presence of planetary companions. The upper chromosphere Hα line extracted following Sect. 2.5 has a value of 0.151 ± 0.002 (arithmetic average and standard deviation).

The tidal evolution of the stellar rotation has a much longer timescale than the age of the system, even considering an extremely strong tidal interaction with a stellar modified tidal quality factor $Q'_\star = 10^5$ (e.g. Mardling & Lin 2002). Therefore, we do not expect tides to affect the estimate of the stellar age based on gyrochronology.

3.5. Rotation period

The extensive datasets we collected allowed us to obtain several estimates of the rotation period of the star, a key parameter for age determination. As mentioned in Sects. 2.1 and 2.2, from the analysis of TESS and ASAS-SN light curves, we obtained photometric periodicities of 7.18 ± 0.21 and 7.34 ± 0.01 days, respectively. The larger error of the determination based on TESS data is due to the short baseline of the monitoring (single sector).

We also exploited the HARPS-N time series of RVs and several spectroscopic indicators (Sect. 2.5). Figure 4 displays the GLS periodograms, computed for the frequency range 0.0001–0.5 days^{-1}, or 2–10 000 days. We removed a linear trend from $\log R'_{\rm HK}$ and Hα time series before running the GLS. The RVs, BIS, and FWHM periodograms show a clear peak (orange line, normalised GLS power >0.2) close to the first harmonic of the stellar rotation period detected using the ASAS-SN photometry (7.34 days, dotted green lines). As the period is compatible with the modulation observed in the photometry and consistently recovered in both the RV and the activity indexes, we associated this signal to the stellar activity. This result could be a sign that RV variations are dominated by dark spots rather than the quenching of convective motions in the magnetised regions of the photosphere, as explained in the study by Lanza et al. (2010). Moreover, the periodograms of Hα and $W_{\rm CCF}$ show peaks that are consistent with the photometric period. On the other hand, the second-highest peak in the RV periodogram reveals

the signal of the validated gas giant planet. We also add that the detailed modelling of the RV time series with Gaussian processing regression (Sect. 4.3) yields a value of 7.37 ± 0.03 days for the rotation period.

In summary, the available photometric and spectroscopic time series consistently indicate a periodicity of 7.34 ± 0.05 days, which we interpret as the rotation period of the star. The shorter periodicity seen in some spectroscopic indicators is fully compatible with being the first harmonic of the true periodicity, as observed in several other cases (see e.g. TOI-1807 Nardiello et al. 2022). Conversely, we think it is unlikely that the true period is the shorter one (3.66 d), with this periodicity arising from the presence of active regions of comparable areas on opposite stellar hemispheres, especially considering the long-time baseline of the ASAS-SN time series.

3.6. Kinematics

Kinematic space velocities were derived adopting *Gaia* kinematic parameters and using the formalism by Johnson & Soderblom (1987). The resulting U, V, and W (Table 2) are at the boundary of the kinematic space of young stars (age younger than about 500 Myr; Montes et al. 2001; Maldonado et al. 2010) in agreement with the other age diagnostics. TOI-5398 is not a member of any of the known young moving groups and a dedicated search of comoving objects within a few degrees in the *Gaia* DR3 catalogue does not yield convincing candidates.

3.7. Age, mass, and radius

The indirect methods discussed above point towards an age of a few hundred million years, similar to the Hyades and Praesepe open clusters, which also have super-solar metallicity (Hyades with +0.15 dex, Cummings et al. 2017, and Praesepe with +0.21 dex, D'Orazi et al. 2020). In the case of a G dwarf star of a few hundred million years old, the most robust age indicator is the rotation period. An age of 680 Myr is obtained with the Mamajek & Hillenbrand (2008) calibration for our adopted rotation period. Using different photometric colours and calibrations (e.g. G-K Messina et al. 2022) yields similar results. The lithium abundance is intermediate between members of Hyades (~650 Myr) and M35 (~200 Myr) of similar colour, pointing to a somewhat younger age. The level of chromospheric activity also suggests a younger age than the gyrochronology, but the discrepancy between both lithium and $\log R'_{\rm HK}$ and the expectations for an age similar to that of the Hyades cluster is marginal. Finally, kinematic parameters are fully consistent with an age of a few hundred million years and the lack of comoving objects prevents a more precise age estimate. We further add that isochrone fitting performed using the `param`[7] tool (da Silva et al. 2006) does not add further relevant information (nominal age 1.6 ± 1.6 Gyr). We therefore adopt a system age of 650 ± 150 Myr from the indirect indicators.

Through the `param` tool and by imposing the age range allowed by indirect methods to avoid the inclusion of solutions not compatible with the above results (Desidera et al. 2015), we derived the stellar mass and radius. We obtained in this way a stellar mass of $1.146 \pm 0.013\ M_\odot$ and a stellar radius of $R = 1.051 \pm 0.013\ R_\odot$, where the uncertainties are those provided by the `param` interface and do not include possible systematic uncertainties in the adopted stellar models.

[7] http://stev.oapd.inaf.it/cgi-bin/param_1.3

Table 2. Stellar properties of TOI-5398.

Parameter	TOI-5398	Ref
α (J2000)	10 47 31.09	*Gaia* DR3
δ (J2000)	+36 19 45.86	*Gaia* DR3
μ_α (mas yr^{-1})	1.360 ± 0.014	*Gaia* DR3
μ_δ (mas yr^{-1})	7.003 ± 0.012	*Gaia* DR3
RV (km s^{-1})	-9.95 ± 0.30	*Gaia* DR3
π (mas)	7.6190 ± 0.0143	*Gaia* DR3
U (km s^{-1})	4.07 ± 0.14	This paper (Sect. 3.6)
V (km s^{-1})	4.90 ± 0.02	This paper (Sect. 3.6)
W (km s^{-1})	-8.83 ± 0.27	This paper (Sect. 3.6)
V (mag)	10.06 ± 0.03	*Tycho*-2 (Høg et al. 2000)
$B - V$ (mag)	0.58	This paper (Sect. 3.4)
G (mag)	9.9875 ± 0.0004	*Gaia* DR3
$G_{BP} - G_{RP}$ (mag)	0.7582	*Gaia* DR3
$J_{\rm 2MASS}$ (mag)	9.026 ± 0.021	2MASS
$H_{\rm 2MASS}$ (mag)	8.772 ± 0.023	2MASS
$K_{\rm 2MASS}$ (mag)	8.713 ± 0.018	2MASS
$T_{\rm eff}$ (K)	6000 ± 75	This paper (spec; Sect. 3.1)
$\log g$	4.44 ± 0.10	This paper (Sect. 3.1)
[Fe/H] (dex)	$+0.09 \pm 0.06$	This paper (Sect. 3.1)
$E(B - V)$ (mag)	≤ 0.024 [(a)]	PIC (Montalto et al. 2021)
$S_{\rm MW}$	0.325 ± 0.008	This paper (Sect. 3.4)
$\log R'_{\rm HK}$	-4.43 ± 0.02	This paper (Sect. 3.4)
$v \sin i_\star$ (km s^{-1})	7.5 ± 0.6	This paper (Sect. 3.2)
$P_{\rm rot}$ (d)	7.34 ± 0.05	This paper (Sect. 3.5)
A(Li)	2.82 ± 0.11	This paper (Sect. 3.3)
Mass ($M_\odot$)	1.146 ± 0.013	This paper (Sect. 3.7)
Radius ($R_\odot$)	1.051 ± 0.013	This paper (Sect. 3.7)
Age (Myr)	650 ± 150	This paper (Sect. 3.7)
$i_\star$ (deg)	≥ 69	This paper (Sect. 3.7)

Notes. [(a)]84th percentile.

From the combination of $R_\star$, $P_{\rm rot}$, and $v \sin i_\star$, we infer a system orientation fully compatible with edge-on. Indeed, for the nominal parameters, $\sin i_\star$ is just below unity, and taking error bars into account, we estimate $i_\star \geq 69$ deg. The stellar parameters outlined in this and the preceding subsections serve as the reference for this study; they are presented in Table 2.

3.8. Spectral energy distribution

As an independent determination of the basic stellar parameters, we performed an analysis of the broadband spectral energy distribution (SED) of the star together with the *Gaia* DR3 parallax (see e.g. Stassun & Torres 2021) in order to determine an empirical measurement of the stellar radius following the procedures described in Stassun & Torres (2016); Stassun et al. (2017, 2018). We obtained the JHK_S magnitudes from 2MASS, the $W1$–$W4$ magnitudes from WISE (Wright et al. 2010), the $G_{\rm BP}\,G_{\rm RP}$ magnitudes from *Gaia* (Gaia Collaboration 2016), and the FUV and NUV magnitudes from GALEX (Martin et al. 2005). Together, the available photometry spans the full stellar SED over the wavelength range 0.2–22 µm (see Fig. 6).

We performed a fit using PHOENIX stellar atmosphere models (Husser et al. 2013), with the free parameters being the effective temperature ($T_{\rm eff}$) and metallicity ([Fe/H]), as well as

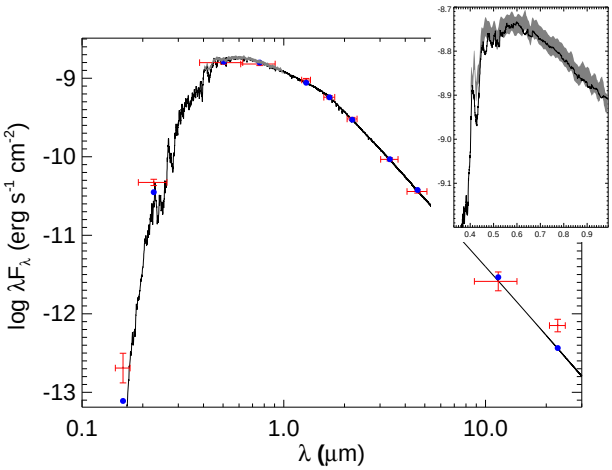

Fig. 6. Spectral energy distribution of TOI-5398. Red symbols represent the observed photometric measurements, where the horizontal bars represent the effective width of the passband. Blue symbols are the model fluxes from the best-fit PHOENIX atmosphere model (black). The *Gaia* spectrum is overlaid as a grey swathe and shown in closer detail in the inset plot.

the extinction A_V, which we limited to a maximum line-of-sight value from the Galactic dust maps of Schlegel et al. (1998). The resulting fit (Fig. 6) has best-fit parameters of $A_V = 0.05 \pm 0.02$ mag, $T_{\rm eff} = 6025 \pm 100$ K, and [Fe/H] $= 0.0 \pm 0.5$, with a reduced χ^2 of 1.3 (excluding the FUV and $W4$ fluxes, which suggest modest excesses in both the UV and mid-IR). Integrating the (unreddened) model SED gives the bolometric flux at Earth, $F_{\rm bol} = 2.470 \pm 0.029 \times 10^{-9}$ erg s^{-1} cm^{-2}. Taking the $F_{\rm bol}$ and $T_{\rm eff}$ together with the *Gaia* parallax gives the stellar radius, $R_\star = 1.059 \pm 0.036\ R_\odot$. In addition, we can estimate the stellar mass from the empirical relations of Torres et al. (2010), obtaining $M_\star = 1.12 \pm 0.07\ M_\odot$. Finally, we may estimate the stellar rotation period from the above radius together with the spectroscopically measured $v \sin i_\star$, giving $P_{\rm rot}/\sin i_\star = 7.1 \pm 0.6$ d. These results are fully compatible with those presented in Sects. 3.1 and 3.7.

4. Analysis

4.1. Planet detection and vetting tests

Two candidate exoplanets orbiting TOI-5398 were identified in Sector 48 light curves in both the SPOC (Jenkins et al. 2016) and QLP (Huang et al. 2020b) pipelines: one giant and one sub-Neptune ($P \sim 10.59$ d and $P \sim 4.77$ d, respectively). The SPOC performed a transit search with an adaptive, noise-compensating matched filter (Jenkins 2002; Jenkins et al. 2010, 2020), producing threshold crossing events (TCEs) for which an initial limb-darkened transit model was fitted (Li et al. 2019) and diagnostic tests were conducted to help assess the planetary nature of the signal (Twicken et al. 2018). The QLP performed its transit search with the Box Least Squares Algorithm (Kovács et al. 2002). The two transit signatures passed all TESS data validation diagnostic tests, and the TESS Science Office issued alerts for TOI-5398.01 (10.59 days) and TOI-5398.02 (4.77 days) on 2022 March 24. The SPOC difference image centroid offsets (Twicken et al. 2018) localised the transit source for TOI 5398.01 within 0.41 ± 2.55 arcsec and for TOI 5398.02 within 2.69 ± 2.67 arcsec; all TIC v8 (Stassun et al. 2019) objects other than TOI-5398 were excluded as the source of each transit signature.

Mantovan et al. (2022) thoroughly validated the planetary nature of the giant, which they label TOI-5398 b, by ruling out any false positive (FP) scenarios capable of mimicking the observed transit signal. More precisely, mainly due to the low spatial resolution of TESS cameras (≈21 arcsec/pixel), some objects initially identified as substellar candidates might be FPs. As a result, vetting and validation tests are critical. Therefore, in order to also better understand the nature of the sub-Neptune candidate, TOI-5398.02, and to exclude FP scenarios, we followed the procedure adopted in Mantovan et al. (2022). The latter approach, further described in Appendix B, considers the major concerns reported in Morton et al. (2023) and ensures reliable results when using VESPA (Morton 2012, 2015). This procedure allowed us to statistically validate the sub-Neptune exoplanet and label it as TOI-5398 c.

4.2. Photometry time-series analysis

To characterise the properties of TOI-5398 b and c, we investigated all the ground-based photometry simultaneously with the two transits of TOI-5398 b and the four transits of TOI-5398 c observed by TESS in a Bayesian framework using `PyORBIT`[8] (Malavolta et al. 2016, 2018), a Python package for modelling planetary transits and RVs while simultaneously accounting for stellar activity effects. The ground-based observations rule out FP scenarios caused by blended eclipsing binaries (BEBs) and further confirm the transits of two planetary companions orbiting TOI-5398.

In the present case, we took our TESS-corrected light curve (see Sect. 2.1) and carefully considered the influence of stellar contamination from neighbouring stars. We verified the stellar dilution by measuring a dilution factor, which defines the total flux from contaminants that fall into the photometric aperture divided by the flux contribution of the target star. Following Sect. 2.2.2 of Mantovan et al. (2022), we determined the dilution factor (and its associated error) by calculating the contribution of the flux that falls into the TESS aperture for each star. We determined its value to be 0.00735 ± 0.00005, and we imposed it as a Gaussian prior in the modelling. We then selected each space-based transit event from the corrected light curve – and an out-of-transit part of equal duration to that of the corresponding transit (both before the ingress and after the egress) – and created a mask that flags each transit and cuts the corresponding portions of the light curve. The transits of the two planets do not overlap.

We simultaneously modelled each transit (ground- and space-based) using the code `BATMAN` (Kreidberg 2015), fitting the following parameters: the central time of transit (T_0), the planetary-to-star radius ratio ($R_p/R_\star$), the impact parameter, b, the stellar density ($\rho_\star$, in solar units), the quadratic limb-darkening (LD) coefficients u_1 and u_2 adopting the LD parametrization (q_1 and q_2) introduced by Kipping (2013), a second-order polynomial trend to take into account the local stellar variability (with c_0 as the intercept, c_1 as the linear coefficient, and c_2 as the quadratic coefficient), and a jitter term to be added in quadrature to the errors of the photometry to account for any effects that were not included in our model (e.g. short-term stellar activity) or any underestimation of the error bars. We applied an airmass detrending technique to each ground-based light curve, and estimated u_1 and u_2 using `PyLDTk`[9] (Husser et al. 2013; Parviainen & Aigrain 2015) and applying the

[8] https://github.com/LucaMalavolta/PyORBIT
[9] https://github.com/hpparvi/ldtk

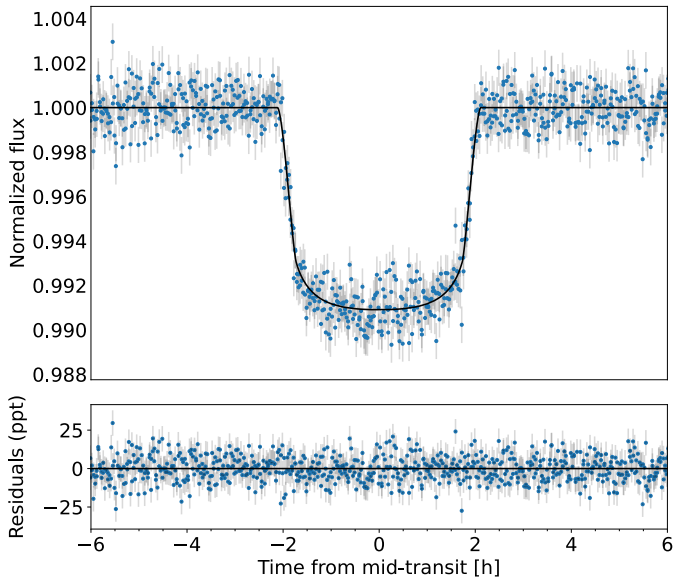

Fig. 7. Photometric modelling of TOI-5398 b planetary signal. In the *top panel*, we display the TESS phase-folded transits after normalisation along with the transit model (black line). In the *panel below*, we show the residuals.

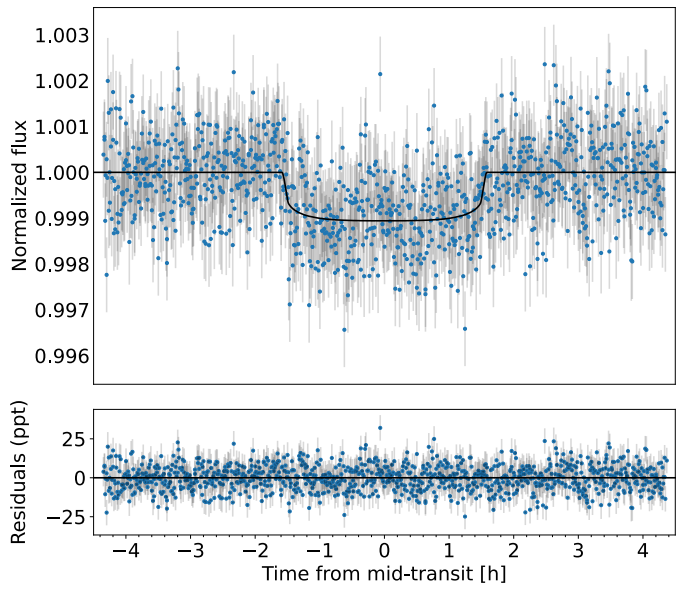

Fig. 8. As in Fig. 7, but for TOI-5398 c.

specific filters used for the observations. We imposed a Gaussian prior on the stellar density, whereas we imposed uniform priors on the period and T_0. We then imposed a Gaussian prior on the eccentricities following Van Eylen et al. (2019).

We performed a global optimisation of the parameters by executing a differential evolution algorithm (Storn & Price 1997, PyDE[10]) and performing a Bayesian analysis of each selected light curve around each transit. The latter was achieved using the affine-invariant ensemble sampler (Goodman & Weare 2010) for Markov chain Monte Carlo (MCMC) implemented within the package EMCEE (Foreman-Mackey et al. 2013). We used $4n_{\rm dim}$ walkers (with $n_{\rm dim}$ being the dimensionality of the model) for 50 000 generations with PyDE and then with 100 000 steps with EMCEE – where we applied a thinning factor of 200 to reduce the effect of the chain auto-correlation. We discarded the first 25 000 steps (burn-in) after checking the convergence of the chains with the Gelman–Rubin (GR) statistics (Gelman & Rubin 1992, threshold value $\hat{\rm R} = 1.01$). Unless specifically stating otherwise, the same sampling configuration and process were used throughout all occurrences of PyDE and EMCEE. Figures 7–9 and Table 3 present the results of the modelling.

4.3. RV time-series analysis

Using PyORBIT, we investigated the RV time-series data in a Bayesian framework. We tried various approaches to model the stellar activity through the use of Gaussian processes (GPs; Rasmussen et al. 2006; Haywood et al. 2014). We experimented with a number of data-set combinations to constrain the GP hyper-parameters and consider various planetary system architectures (one, two, or more planets). Here we outline the three most notable cases.

Due to the high computational cost of the GPs, we only modelled the spectroscopic time series in each test. However, we included the inclination from the photometry model to determine the true masses.

[10] https://github.com/hpparvi/PyDE

4.3.1. *Case 1: Two-planet system and activity modelling trained on spectroscopy: Uni-dimensional GP*

In the first case, we tested a multi-planet system model formed by TOI-5398 b and TOI-5398 c. PyORBIT simultaneously modelled the stellar activity and the signals of the two planets in the RV series. In the model, we included the inclination measured from photometry and the stellar mass $M_\star$ as derived in Sect. 3 to determine the true masses of the planets. We then imposed a Gaussian prior on the eccentricities following Van Eylen et al. (2019) and included the RV semi-amplitudes $K_{\rm b}$ and $K_{\rm c}$ in the RV modelling. Moreover, we used Gaussian priors on both orbital periods ($P_{\rm b}$, $P_{\rm c}$) and central time of the first transits ($T_{0,\rm b}$, $T_{0,\rm c}$) by considering the parameters outlined in Sect. 4.2.

We modelled the stellar activity in the RV, BIS, and $\log R'_{HK}$ series simultaneously through a GP regression. We used a quasi-periodic kernel as defined by Grunblatt et al. (2015). As part of this modelling, we set the stellar rotation period $P_{\rm rot}$ (Gaussian prior, as defined in Sect. 2.2), the characteristics decay timescale $P_{\rm dec}$, and the coherence scale w. In accordance with Eastman et al. (2013), we fitted the periods and semi-amplitudes of the RV signals in the linear space, and determined the eccentricity e and the argument of periastron ω by fitting $\sqrt{e}\cos\omega$ and $\sqrt{e}\sin\omega$. We performed a global optimisation of the parameters by running PyDE and performing a Bayesian analysis of the planetary signals and activity in the RV time series using EMCEE. The results of this analysis are discussed below our presentation of each respective case in Sect. 4.3.3 and in Table 4.

4.3.2. *Case 2: Two-planet system and activity modelling trained on spectroscopy: Multidimensional GP*

In the present case, we modelled the stellar activity of TOI-5398 using the multidimensional GP framework developed by Rajpaul et al. (2015) and reimplemented in PyORBIT in accordance with the prescriptions in the paper (see also Barragán et al. 2022). Again, we relied on the quasi-periodic kernel and its derivatives. We modelled RV, BIS, and $\log R'_{HK}$ spectroscopic time series.

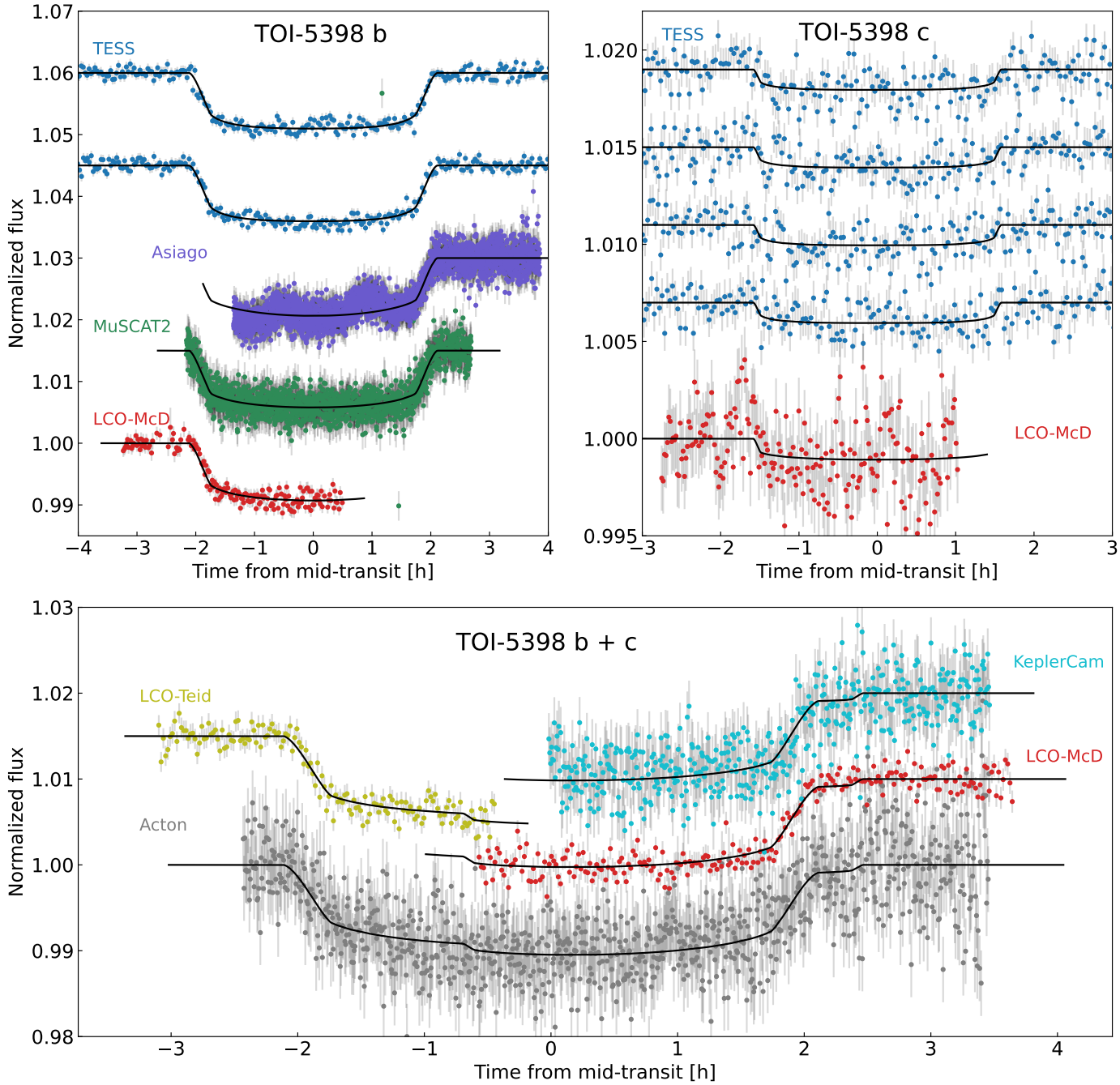

Fig. 9. Ground-based photometric data simultaneously modelled with TESS transits. Different datasets are represented by distinct colours. *Top*: Individual transits of TOI-5398 b on the left and TOI-5398 c on the right. *Bottom*: Simultaneous transit of TOI-5398 b and c observed during the night of 2022 April 21.

The three-dimensional GP model is the following:

$$\begin{aligned} \Delta RV &= V_c\, G(t) + V_r\, \dot{G}(t), \\ \log R'_{HK} &= L_c\, G(t), \\ BIS &= B_c\, G(t) + B_r\, \dot{G}(t), \end{aligned} \tag{1}$$

where $G(t)$ is the GP and $\dot{G}(t)$ its time derivative. The constants denoted by subscripts r and c represent free parameters linking the individual time series to $G(t)$ and $\dot{G}(t)$ (Barragán et al. 2023).

To perform the modelling with PyORBIT, we assigned the same priors described in Case 1 to planets and stellar parameters. Then, we ran a global optimisation of the parameters with PyDE and a Bayesian analysis of the planetary signals and activity in the RV time series with EMCEE. The results of this analysis are discussed below, following a presentation of each respective case, and in Table 4.

4.3.3. Case 3: *Extended list of activity indexes and search for a third planet*

To better disentangle planetary and stellar signals, we extended the list of activity indexes that PyORBIT simultaneously models with the two Keplerian signals (described in Case 2). In particular, we included the chromospheric activity indicator Hα

Table 3. Priors and outcomes of the model of planet b and c from the analysis of the photometric time series.

Photometric time-series fit			
Parameter	Unit	Prior	Value
Stellar density ($\rho_\star$)	$\rho_\odot$	$\mathcal{U}(0.75, 10.25)$	$0.971^{+0.042}_{-0.049}$
TESS dilution factor		$\mathcal{N}(0.00735, 0.00005)$	0.007348 ± 0.000050
TESS jitter ($\sigma^{\rm TESS}_{\rm jitter}$)	$e^- \, s^{-1}$	...	$5.0^{+1.1}_{-1.4}$
Asiago jitter ($\sigma^{\rm Asiago}_{\rm jitter}$)		...	$0.00074^{+0.00006}_{-0.00007}$
LCO_McD_c jitter ($\sigma^{\rm McD_c}_{\rm jitter}$)		...	$0.00145^{+0.00011}_{-0.00010}$
LCO_McD_b jitter ($\sigma^{\rm McD_b}_{\rm jitter}$)		...	$0.00073^{+0.00009}_{-0.00008}$
MuSCAT2 jitter ($\sigma^{\rm MuSCAT2}_{\rm jitter}$)		...	$0.00014^{+0.00012}_{-0.00008}$
KeplerCam jitter ($\sigma^{\rm KeplerCam}_{\rm jitter}$)		...	$0.00279^{+0.00011}_{-0.00010}$
Acton jitter ($\sigma^{\rm Acton}_{\rm jitter}$)		...	0.00349 ± 0.00010
LCO_McD_bc jitter ($\sigma^{\rm McD_bc}_{\rm jitter}$)		...	$0.00095^{+0.00008}_{-0.00008}$
LCO_Teid jitter ($\sigma^{\rm Teid}_{\rm jitter}$)		...	$0.00067^{+0.00012}_{-0.00013}$
TESS quadratic LD coefficient ($u_1^{\rm TESS}$)		$\mathcal{U}(0, 1)$	$0.089^{+0.089}_{-0.061}$
TESS quadratic LD coefficient ($u_2^{\rm TESS}$)		$\mathcal{U}(0, 1)$	$0.52^{+0.11}_{-0.14}$
Asiago quadratic LD coefficient ($u_1^{\rm Asiago}$)		$\mathcal{N}(0.489, 0.014)$	0.455 ± 0.013
Asiago quadratic LD coefficient ($u_2^{\rm Asiago}$)		$\mathcal{N}(0.151, 0.037)$	$0.007^{+0.033}_{-0.032}$
McD_c quadratic LD coefficient ($u_1^{\rm McD_c}$)		$\mathcal{N}(0.34, 0.01)$	0.340 ± 0.010
McD_c quadratic LD coefficient ($u_2^{\rm McD_c}$)		$\mathcal{N}(0.14, 0.03)$	0.14 ± 0.03
McD_b quadratic LD coefficient ($u_1^{\rm McD_b}$)		$\mathcal{N}(0.34, 0.01)$	0.343 ± 0.010
McD_b quadratic LD coefficient ($u_2^{\rm McD_b}$)		$\mathcal{N}(0.14, 0.03)$	0.17 ± 0.03
MuSCAT2 quadratic LD coefficient ($u_1^{\rm MuSCAT2}$)		$\mathcal{N}(0.34, 0.01)$	0.337 ± 0.010
MuSCAT2 quadratic LD coefficient ($u_2^{\rm MuSCAT2}$)		$\mathcal{N}(0.14, 0.03)$	0.13 ± 0.03
KeplerCam quadratic LD coefficient ($u_1^{\rm KeplerCam}$)		$\mathcal{N}(0.34, 0.01)$	0.334 ± 0.010
KeplerCam quadratic LD coefficient ($u_2^{\rm KeplerCam}$)		$\mathcal{N}(0.14, 0.03)$	0.10 ± 0.03
Acton quadratic LD coefficient ($u_1^{\rm Acton}$)		$\mathcal{N}(0.40, 0.01)$	0.4013 ± 0.0099
Acton quadratic LD coefficient ($u_2^{\rm Acton}$)		$\mathcal{N}(0.14, 0.03)$	0.15 ± 0.03
McD_bc quadratic LD coefficient ($u_1^{\rm McD_bc}$)		$\mathcal{N}(0.34, 0.01)$	0.340 ± 0.010
McD_bc quadratic LD coefficient ($u_2^{\rm McD_bc}$)		$\mathcal{N}(0.14, 0.03)$	0.14 ± 0.03
Teid quadratic LD coefficient ($u_1^{\rm Teid}$)		$\mathcal{N}(0.34, 0.01)$	0.339 ± 0.010
Teid quadratic LD coefficient ($u_2^{\rm Teid}$)		$\mathcal{N}(0.14, 0.03)$	0.14 ± 0.03
Planet b			
Parameter	Unit	Prior	Value
Orbital period ($P_{\rm b}$)	days	$\mathcal{U}(10.57, 10.61)$	$10.590547^{+0.000012}_{-0.000011}$
Central time of the first transit ($T_{0,\rm b}$)	BTJD	$\mathcal{U}(2616.4, 2616.6)$	$2616.49232^{+0.00022}_{-0.00021}$
Semi-major axis to stellar radius ratio ($a_{\rm b}/R_\star$)		...	20.0 ± 0.6
Orbital semi-major axis ($a_{\rm b}$)	au	...	0.098 ± 0.005
Orbital inclination (i)	deg	...	$89.21^{+0.31}_{-0.21}$
Orbital eccentricity ($e_{\rm b}$)		$\mathcal{N}(0, 0.098)$	$\leqslant 0.094$ [a]
Impact parameter (b)		$\mathcal{U}(0, 1)$	$0.272^{+0.069}_{-0.110}$
Transit duration (T_{14})	days	...	$0.1774^{+0.0062}_{-0.0043}$
Planetary radius ($R_{\rm b}$)	$R_\oplus$	...	10.30 ± 0.40
Planet c			
Parameter	Unit	Prior	Value
Orbital period ($P_{\rm c}$)	days	$\mathcal{U}(4.770, 4.776)$	$4.77271^{+0.00016}_{-0.00014}$
Central time of the first transit ($T_{0,\rm c}$)	BTJD	$\mathcal{U}(2628.5, 2628.7)$	$2628.61781^{+0.00090}_{-0.00086}$
Semi-major axis to stellar radius ratio ($a_{\rm c}/R_\star$)		...	11.8 ± 0.4

Table 3. continued.

Planet c			
Parameter	Unit	Prior	Value
Orbital semi-major axis (a_c)	au	...	0.057 ± 0.003
Orbital inclination (i)	deg	...	$\geqslant 88.40$ [(b)]
Orbital eccentricity (e_c)		$\mathcal{N}(0, 0.098)$	$\leqslant 0.117$ [(a)]
Impact parameter (b)		$\mathcal{U}(0, 1)$	$\leqslant 0.34$ [(a)]
Transit duration (T_{14})	days	...	$0.1303^{+0.0042}_{-0.0053}$
Planetary radius (R_c)	$R_\oplus$	...	3.52 ± 0.19

Notes. [(a)]84th percentile. [(b)]16th percentile.

(Gomes da Silva et al. 2011) as well as the two CCF asymmetry diagnostics FWHM and equivalent width $W_{\rm CCF}$.

On the one hand, the Hα line complements the lower chromosphere indicator $\log R'_{\rm HK}$ by providing information about the conditions in the upper chromosphere of a star (Gomes da Silva et al. 2011). More specifically, Hα and Ca H & K are emitted from different depths – and are formed at different temperatures – in the chromosphere (Robertson et al. 2013; Gomes da Silva et al. 2014). Therefore, it is helpful to study the Hα and $\log R'_{\rm HK}$ indices simultaneously (Gomes da Silva et al. 2011, 2014) to learn more about the presence of distinct activity-related features and disentangle their signals from Keplerian ones in the RV time series. On the other hand, according to 3 yr of RV monitoring of the Sun (Collier Cameron et al. 2019), the line-shape parameters of the CCF appear to respond to different components of the active regions. Moreover, they help to track global temperature changes in the photosphere (see also Malavolta et al. 2017).

For the reasons listed, we decided to include both the chromospheric indicators Hα and $\log R'_{\rm HK}$ in the modelling, as well as the three CCF asymmetry diagnostics BIS, FWHM, and $W_{\rm CCF}$. We followed the multi-dimensional GP formalism introduced by Rajpaul et al. (2015) to examine the RV and BIS time series, using the first derivative of the GP. Conversely, we did not use the first derivative for the remaining four time series, as suggested also in Barragán et al. (2023). The six-dimensional GP model is an extension of Eq. (1), with the addition of the following supplementary terms:

$$\begin{aligned} {\rm H}\alpha &= L2_{\rm c}\, G(t) \\ FWHM &= L3_{\rm c}\, G(t), \\ W_{\rm CCF} &= L4_{\rm c}\, G(t). \end{aligned} \tag{2}$$

We performed the modelling with `PyORBIT` in the same way as described in the previous cases, and we show the outcomes in Figs. 10, 11, and Table 5.

We emphasise that the inclusion of the additional activity indicators reduces the uncertainties in the Keplerian signals and the RV jitter term with respect to Case 1 and Case 2. Notably, the orbital parameters remain consistent across all cases. We used the Bayesian information criterion (BIC, Schwarz 1978) to compare the first two cases. Our analysis revealed a strong preference for Case 2 over Case 1, with a substantial $\Delta{\rm BIC}_{12}$ value of 148 (Kass & Raftery 1995). In general, the BIC may not be the optimal estimator for the Bayesian evidence; however, in this specific case, we believe that the extreme difference between the BIC values (ΔBIC = 148) largely overcomes any possible bias, thus favouring Case 2 over Case 1. Regarding Case 3, a direct BIC comparison is not possible due to the different datasets employed in the analysis. Instead, based on logical grounds, we selected Case 3 as our reference model. Each additional activity indicator provides valuable information on specific aspects of stellar activity, as evidenced in previous paragraphs, and their inclusion is justified by the amplitude parameter of the covariance matrix being significantly different from zero for every extra activity indicator; that is, those activity indicators further constrain the activity model independently from the observed RVs. The adopted masses for planets b and c are $58.7^{+5.7}_{-5.6}$ and $11.8^{+4.8}_{-4.7}\, M_\oplus$, respectively. We include the final parameters of planets b and c in Table 6, while Table 4 lists the differences between this model and the other two. The significantly reduced jitter observed in Cases 2 and 3 compared to Case 1 may be attributed to the limited capability of the uni-dimensional GP framework to model the different periodicities present in the spectroscopic time series. In particular, the RV and chromospheric indexes exhibit different periodicities (see also Sect. 3.5 and Fig. 4) when the RV variations are dominated by dark spots. In contrast, Cases 2 and 3 use the formalism outlined in Rajpaul et al. (2015), which effectively handles variations in periodicity.

Table 4. Comparison of the three different models.

Parameter	Case 1	Case 2	Case 3
$K_{\rm b}$ (m s^{-1})	14.0 ± 2.7	14.8 ± 1.7	15.7 ± 1.5
$K_{\rm c}$ (m s^{-1})	$3.9^{+2.7}_{-2.4}$	$3.1^{+1.7}_{-1.6}$	$4.1^{+1.6}_{-1.7}$
$\sigma^{\rm RV}_{\rm jitter}$ (m s^{-1})	$8.3^{+7.3}_{-6.2}$	$1.8^{+2.0}_{-1.2}$	$1.5^{+1.6}_{-1.1}$

In addition to the modelling mentioned above, we looked for the presence of a third planet in our RV dataset by applying wide uniform priors on its period P and RV semi-amplitude K. While we did not impose that the orbit of the third planet be circular, we applied a Gaussian prior on the eccentricity following Van Eylen et al. (2019). Initially, the global optimisation algorithm and the first ten thousand steps of the MCMC exploration suggested a significant detection of a third planet. However, the chains of the planet's orbital period diverged relatively early on, preventing us from claiming a third planet detection. We underline that the solutions for planets b and c in the system show little variation, which further strengthens the validity of their detections.

Table 5. Priors and outcomes of the model of planets b and c from analysing spectroscopic series with a multi-dimensional GP framework (Case 3).

GP framework parameters			
Parameter	Unit	Prior	Value
Uncorrelated RV jitter ($\sigma^{\rm RV}_{\rm jitter,0}$)	m s^{-1}	...	$1.5^{+1.6}_{-1.1}$
RV offset ($\gamma_0^{\rm RV}$)	m s^{-1}	...	$-9432.9^{+2.9}_{-2.8}$
Uncorrelated BIS jitter ($\sigma^{\rm BIS}_{\rm jitter,0}$)	m s^{-1}	...	$17.1^{+1.7}_{-1.6}$
BIS offset ($\gamma_0^{\rm BIS}$)	m s^{-1}	...	$10.6^{+2.6}_{-2.6}$
Uncorrelated log R'_{HK} jitter ($\sigma^{\log R'_{\rm HK}}_{\rm jitter,0}$)		...	$0.0127^{+0.0014}_{-0.0013}$
log R'_{HK} offset ($\gamma_0^{\log R'_{\rm HK}}$)		...	-4.4137 ± 0.0030
Uncorrelated Hα jitter ($\sigma^{\rm H\alpha}_{\rm jitter,0}$)		...	0.0017 ± 0.0002
Hα offset ($\gamma_0^{\rm H\alpha}$)		...	0.1513 ± 0.0004
Uncorrelated FWHM jitter ($\sigma^{\rm FWHM}_{\rm jitter,0}$)	km s^{-1}	...	0.046 ± 0.004
FWHM offset ($\gamma_0^{\rm FWHM}$)	km s^{-1}	...	11.37 ± 0.01
Uncorrelated $W_{\rm CCF}$ jitter ($\sigma^{W_{\rm CCF}}_{\rm jitter,0}$)	km s^{-1}	...	$0.0013^{+0.0013}_{-0.0009}$
$W_{\rm CCF}$ offset ($\gamma_0^{W_{\rm CCF}}$)	km s^{-1}	...	3.505 ± 0.003
Multidimensional GP parameters (Rajpaul et al. 2015)			
V_c	m s^{-1}	$\mathcal{U}(-100.0, 100.0)$	$-11.2^{+2.3}_{-2.8}$
V_r	m s^{-1}	$\mathcal{U}(0.0, 100.0)$	$27.1^{+4.3}_{-3.6}$
B_c	m s^{-1}	$\mathcal{U}(-100.0, 100.0)$	$4.3^{+3.3}_{-3.2}$
B_r	m s^{-1}	$\mathcal{U}(-100.0, 100.0)$	$-35.6^{+4.8}_{-6.0}$
L_c (log R'_{HK})		$\mathcal{U}(-0.1, 0.1)$	-0.011 ± 0.002
$L2_c$ (Hα)		$\mathcal{U}(-0.1, 0.1)$	-0.0015 ± 0.0003
$L3_c$ (FWHM)	km s^{-1}	$\mathcal{U}(-0.5, 0.5)$	$-0.043^{+0.007}_{-0.008}$
$L4_c$ ($W_{\rm CCF}$)	km s^{-1}	$\mathcal{U}(-0.02, 0.02)$	-0.014 ± 0.002
Stellar activity (RV + activity indexes)			
Parameter	Unit	Prior	Value
Rotational period ($P_{\rm rot}$)	days	$\mathcal{N}(7.34, 0.15)$	7.37 ± 0.03
Decay Timescale of activity ($P_{\rm dec}$)	days	$\mathcal{U}(10.0, 2000.0)$	$26.1^{+3.3}_{-3.0}$
Coherence scale (w)		$\mathcal{U}(0.01, 0.60)$	0.36 ± 0.03
Planet b			
Parameter	Unit	Prior	Value
Orbital period ($P_{\rm b}$)	days	$\mathcal{N}(10.590547, 0.000012)$	10.590547 ± 0.000012
Central time of the first transit ($T_{0,\rm b}$)	BTJD	$\mathcal{N}(2616.49232, 0.00022)$	2616.49232 ± 0.00022
Orbital eccentricity ($e_{\rm b}$)		$\mathcal{N}(0.00, 0.098)$	$\leqslant 0.13$
Argument of periastron ($\omega_{\rm b}$)	deg	...	92^{+82}_{-45}
Semi-major axis to stellar radius ratio ($a_{\rm b}/R_\star$)		...	20.2 ± 0.3
Orbital semi-major axis ($a_{\rm b}$)	au	...	0.0988 ± 0.0004
RV semi-amplitude ($K_{\rm b}$)	m s^{-1}	$\mathcal{U}(0.01, 100.0)$	$15.7^{+1.5}_{-1.5}$
Planetary mass ($M_{\rm p,b}$)	$M_\oplus$	...	$58.7^{+5.7}_{-5.6}$
Planet c			
Parameter	Unit	Prior	Value
Orbital period ($P_{\rm c}$)	days	$\mathcal{N}(4.77271, 0.00016)$	4.77270 ± 0.00016
Central time of the first transit ($T_{0,\rm c}$)	BTJD	$\mathcal{N}(2628.6178, 0.0009)$	2628.6178 ± 0.0009
Orbital eccentricity ($e_{\rm c}$)		$\mathcal{N}(0.00, 0.098)$	$\leqslant 0.14$
Argument of periastron ($\omega_{\rm c}$)	deg	...	172^{+79}_{-107}
Semi-major axis to stellar radius ratio ($a_{\rm c}/R_\star$)		...	11.9 ± 0.2
Orbital semi-major axis ($a_{\rm c}$)	au	...	0.0581 ± 0.0002
RV semi-amplitude ($K_{\rm c}$)	m s^{-1}	$\mathcal{U}(0.01, 100.0)$	$4.1^{+1.7}_{-1.6}$
Planetary mass ($M_{\rm p,c}$)	$M_\oplus$	...	$11.8^{+4.8}_{-4.7}$

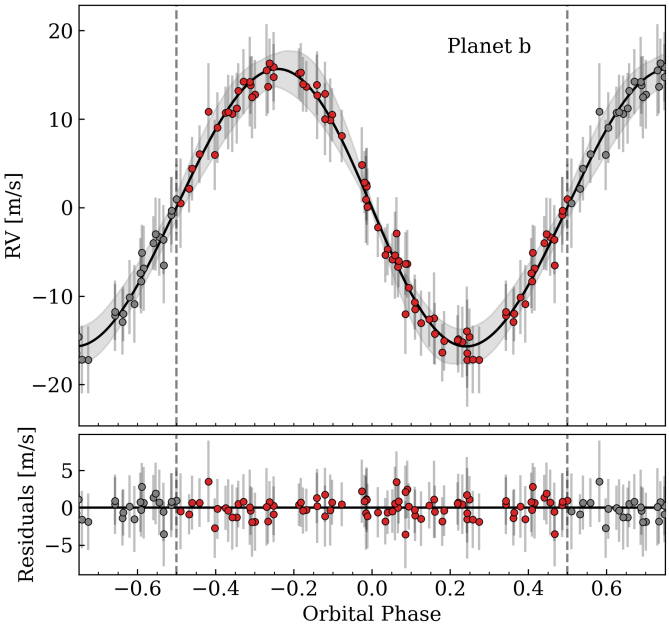

Fig. 10. Phase-folded RV fit of TOI-5398 b planetary signal. The reported error bars include the jitter term, added in quadrature. The shaded area represents the $\pm 1\sigma$ uncertainties of the RV model. The *bottom panel* displays the residuals of the fit.

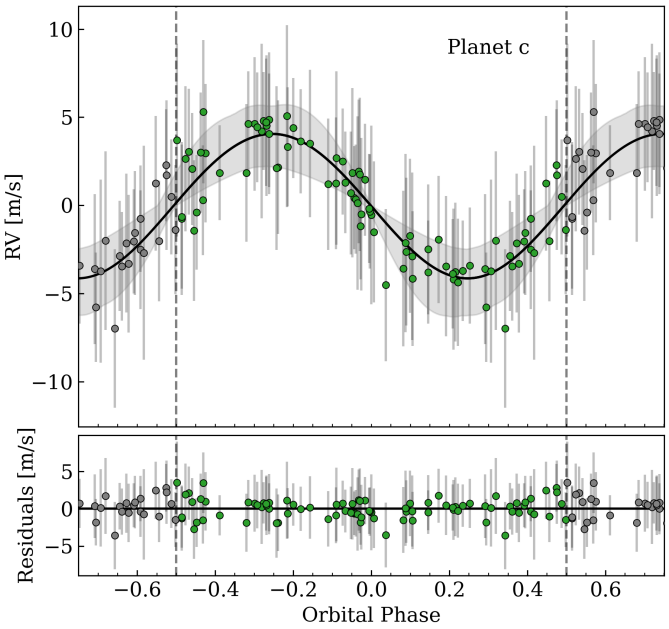

Fig. 11. As in Fig. 10, but for planet c.

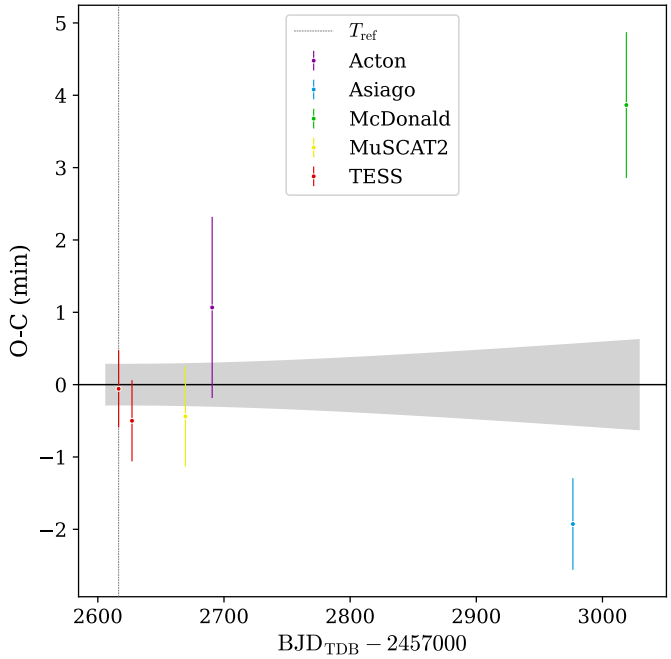

Fig. 12. O-C plot representing the observed (O) and calculated (C) transit times for the linear ephemeris of TOI-5398 b (see Table 6). Each dataset is shown in a distinct colour.

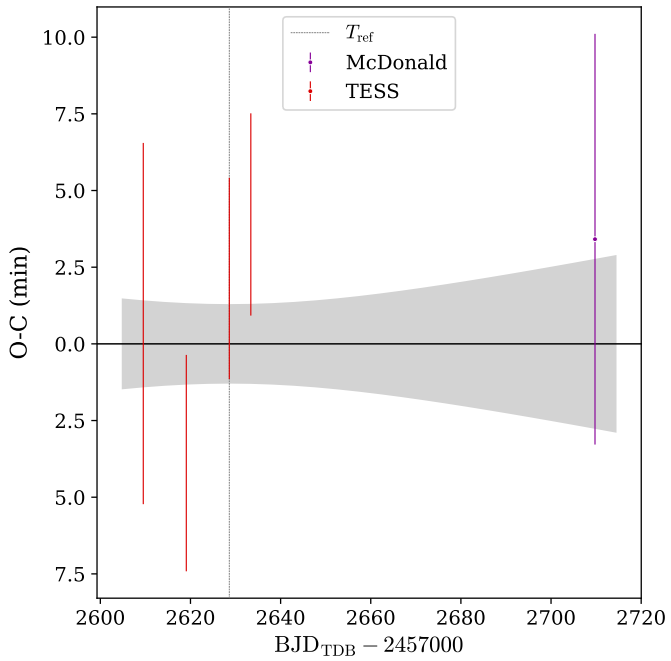

Fig. 13. As in Fig. 12, but for TOI-5398 c.

4.4. Search for transit timing variations

To investigate the potential presence of dynamical interactions between TOI-5398 b and c, we performed a search for transit timing variations (TTVs; e.g. Agol et al. 2005; Holman & Murray 2005; Borsato et al. 2014, 2019, 2021) of planets b and c.

We computed the observed (O) – calculated (C) diagrams for both planets, removing the linear ephemeris (in Table 6) to each transit time. See the O-C diagrams in Figs. 12 and 13 for planets b and c, respectively. The possible TTV amplitude ($A_{\rm TTV}$), computed as the semi-amplitude of the O-C, is of $2.9^{+1.2}_{-1.0}$ min for planet b and 4^{+7}_{-2} min for planet c. The associated error is derived from the subtraction of $A_{\rm TTV}$ from the high-density interval at 95% of a Monte Carlo sampling of 10 000 repetitions.

Although our data do not cover a sufficient portion of the super-period to offer direct evidence, they do suggest a possible TTV due to the gravitational interaction of planets b and c (see Fig. 12). The sparse sampling of the TTV signals prevented us from running a dynamical fit, and so we decided to run a forward dynamical model with `TRADES`[11] (Borsato et al. 2014, 2019, 2021) similar to that presented by Tuson et al. (2023). We took

[11] https://github.com/lucaborsato/trades

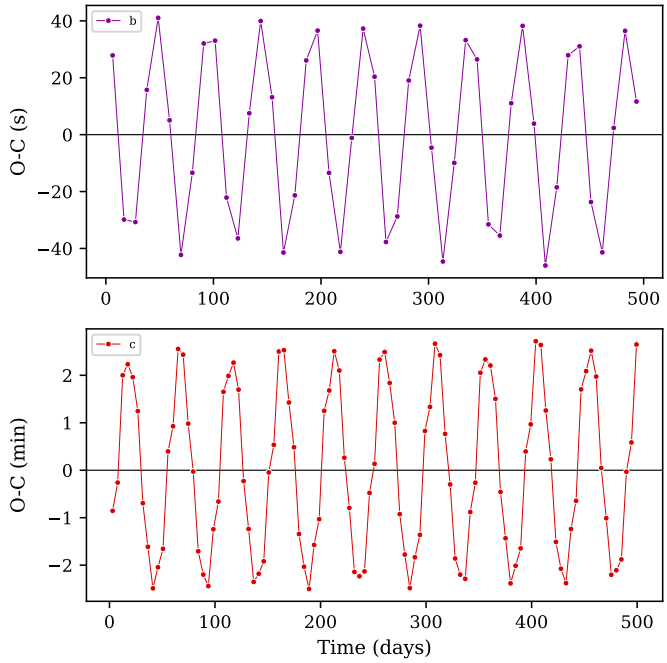

Fig. 14. Synthetic O-C diagrams (*top-panel* planet b, *bottom-panel* planet c) computed from the dynamical simulation with TRADES and with parameters from Table 5.

Table 6. Final parameters of the multi-planet system TOI-5398.

Parameter	TOI-5398 b	TOI-5398 c
P (days)	$10.590547^{+0.000012}_{-0.000011}$	$4.77271^{+0.00016}_{-0.00014}$
T_0 (BTJD)	$2616.49232^{+0.00022}_{-0.00021}$	$2628.61781^{+0.00090}_{-0.00086}$
$a/R_\star$	20.0 ± 0.6	11.8 ± 0.4
a (au)	0.098 ± 0.005	0.057 ± 0.003
$R_p/R_\star$	$0.0899^{+0.0007}_{-0.0006}$	$0.0308^{+0.0011}_{-0.0012}$
R_p ($R_\oplus$)	10.30 ± 0.40	3.52 ± 0.19
b	$0.272^{+0.069}_{-0.110}$	$\leqslant 0.34$ [(a)]
i (deg)	$89.21^{+0.31}_{-0.21}$	$\geqslant 88.4$ [(b)]
T_{14} (h)	$4.258^{+0.149}_{-0.103}$	$3.127^{+0.108}_{-0.127}$
e	$\leqslant 0.13$ [(a)]	$\leqslant 0.14$ [(a)]
K (m s^{-1})	15.7 ± 1.5	$4.1^{+1.7}_{-1.6}$
M_p ($M_\oplus$)	$58.7^{+5.7}_{-5.6}$	$11.8^{+4.8}_{-4.7}$
ρ_p (g cm^{-3})	0.29 ± 0.05	1.50 ± 0.68
g (m s^{-2})	5.36 ± 0.86	8.99 ± 3.76
T_{eq} (K)	947 ± 28	1242 ± 37

Notes. [(a)]84th percentile. [(b)]16th percentile.

the masses and the orbital parameters from Tables 5 and 6 and we integrated the orbits for about 500 days and computed the transit times of each planet. We computed the O-C diagrams (see Fig. 14) and found that the simulated A_{TTV} is of the order of ~40 s and of ~2 min for planets b and c, respectively.

We used the orbital parameters from Table 6 as the starting point of the dynamical simulation; that is, we assumed that the value we obtained from our global fit spanning about 500 days represents a specific configuration in time, which may not be true. The amplitude of the simulated TTVs may also be dependent on the eccentricity of the two planets. Nevertheless, the outcome of the simulation is compatible (at 2σ for b and at 1σ for c) with the measured TTVs. The scope of this analysis is to show that TTVs can indeed be present in this system, while a full dynamical analysis is outside the scope of this paper and is left to future work.

5. Discussion

5.1. Peculiar architecture

TOI-5398 is a compact multi-planet system composed of a warm giant (TOI-5398 b, $P_{orb} \sim 10.59$ d) and a hot sub-Neptune planet (TOI-5398 c, $P_{orb} \sim 4.77$ d) orbiting a moderately young solar-analogue star. The peculiarity of this system resides in its compactness and planetary architecture, which are uncommon among known multi-planet systems with short-period giant planets. Moreover, the sub-Neptune is the closest planet to the host star. There are currently very few notable examples of compact systems consisting of an inner orbit small-size planet and an outer short-period giant companion (e.g. Hord et al. 2022). The most famous multi-planet system with similar characteristics is WASP-47 (Hellier et al. 2012; Becker et al. 2015; Nascimbeni et al. 2023). Within this family of peculiar planetary systems, we also find Kepler-730 (Zhu et al. 2018; Cañas et al. 2019), TOI-1130 (Huang et al. 2020a; Korth et al. 2023), TOI-2000 (Sha et al. 2023), and WASP-132 (Hord et al. 2022). We list these systems in Table 7, together with a list of available datasets and a few notable parameters that we want to highlight.

Among these compact systems, TOI-5398 stands out, along with WASP-47 and TOI-2000, due to its precise transit photometry and RV measurements. These observations enable the precise measurement of planetary bulk densities and make it an extremely appealing target for continued monitoring with follow-up observations and surveys, including PLATO and Ariel, along with telescopes like the ELT. Moreover, TOI-5398 is the youngest compact system with a gas giant ever confirmed with a relatively good age estimation.

5.2. Variety among compact multi-planet systems

In Fig. 15, we show the architecture of compact multi-planet systems with small-size planets orbiting interior to short-period giant planets ($P \lesssim 10$ d). For comparison, we show the next three systems with giants whose orbital periods are $P < 25$ d (Butler et al. 1997; Bourrier et al. 2018; Weiss et al. 2013; Nesvorný et al. 2013). The semicircular dots represent the host stars, colour-coded by their age, while their sizes encode their radii. Planets, on the other hand, are colour-coded by their equilibrium temperature T_{eq}, and their sizes reflect their planetary masses. The inner planet of WASP-132 and the Kepler-730 planets do not yet have mass measurements, and so we extracted these following Wolfgang et al. (2016) or we show upper limits (Hord et al. 2022).

TOI-5398 hosts the youngest gas giant planet with $P < 25$ d and $M_p > 1/2\ M_{Saturn}$ that is known to have an inner companion. The gas giant TOI-5398 b has a radius similar to Jupiter and a mass close to two-thirds that of Saturn, which is the smallest mass among the giants in compact systems. As a result, its bulk density is around half that of Saturn and roughly equal to that of TOI-1130 c (0.38 g cm^{-3}, Huang et al. 2020a). These properties, as well as its orbital period, make TOI-5398 b quite similar to the hot-Saturn planet TOI-2000 c, while they are in contrast with the properties of the larger WASP-47 b, Kepler-730 b, and TOI-1130 c, which all have radii of ~1.1 R_J and masses of ~1 M_J (apart from Kepler-730 b, for which there is not yet a mass measurement). However, the larger radius and smaller

Table 7. Confirmed compact multi-planet systems, sorted by age.

System	n° known planets	Transiting planets	PRV [(a)]	TTV [(b)]	TSM [(c)]	Age (Gyr)	Reference
TOI-5398	2	True, 2/2	True	Potential	288	0.65 ± 0.15	This paper (Sect. 3.7)
WASP-132	2	True, 2/2	True, 1/2	False	106	3.2 ± 0.5	Hord et al. (2022)
TOI-2000	2	True, 2/2	True	Potential	68	5.3 ± 2.7	Sha et al. (2023)
WASP-47	4	True, 4/4	True	True	47	$6.5^{+2.6}_{-1.2}$	Hellier et al. (2012)
TOI-1130	2	True, 2/2	True	True	345	$8.2^{+3.8}_{-4.9}$	Huang et al. (2020a)
Kepler-730	2	True, 2/2	False	False	25	$9.5^{+2.5}_{-2.7}$	Zhu et al. (2018)

Notes. [(a)]Precise radial velocity. [(b)]Transit time variations. [(c)]Transmission spectroscopy metric of the giant planet in the system.

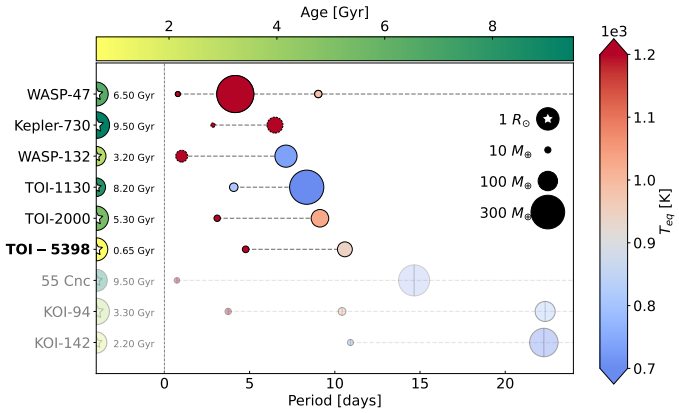

Fig. 15. Architecture of compact multi-planet systems hosting small-size planets orbiting inner to short-period gas giants ($P \lesssim 10$ d). Each row represents one planetary system (y-axis) and the planetary orbital periods (x-axis). The sizes of the dots correspond to the planet masses, and the colours of the points to the equilibrium temperatures (see colour bar to the right). From top to bottom, the systems are sorted in ascending order of the period of the giant. Shaded dots represent the next three systems with gas giants on $P < 25$ d orbits. Dots with a vertical line represent planets whose mass is multiplied by sin(i). The semi-circular dots filled with a star shape indicate the host stars; these are colour-coded by age (see colour bar at the top), while their sizes encode their radii.

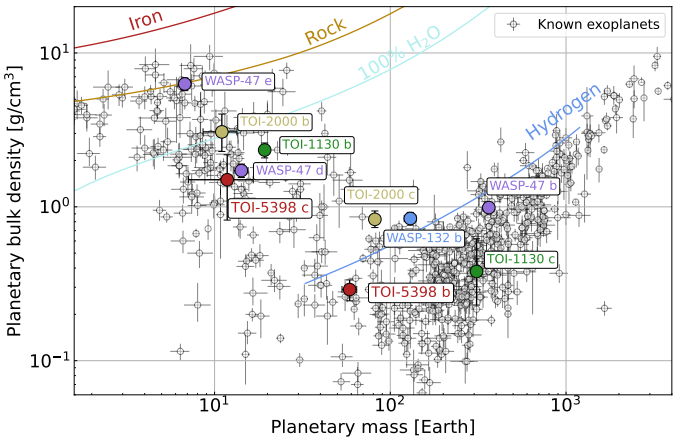

Fig. 16. Mass–density distribution of all confirmed planets from the NASA Exoplanet Archive with mass and radius determinations of better than 20%. The red dots represent TOI-5398 b and c, while the remaining planets mentioned in Table 7 are represented by dots of different colour. We also plot theoretical mass–radius curves for planets of various pure compositions from Zeng et al. (2019, online at `https://lweb.cfa.harvard.edu/~lzeng/planetmodels.html`): solid red indicates a pure-iron core, brown an Earth-like rocky core (32.5% Fe and 67.5% MgSiO3), light blue a 100% water world at 1000 K, and blue a 100% cold-hydrogen world.

mass of TOI-5398 b compared to those of TOI-2000 c – which result in it having a relatively low density compared to giant planets of similar mass (see Fig. 16 and cf., for example, Yee et al. 2022) – mean that the giant planet under study is more like a puffy Saturn (Naponiello et al. 2022). Moreover, we calculated the equilibrium temperature $T_{\rm eq}$ (cf. Eq. (4) from Cowan & Agol 2011) of TOI-5398 b, assuming zero albedo and full day–night heat redistribution following

$$T_{\rm eq} = T_{\rm eff} \sqrt{\frac{R_\star}{a}} \left(\frac{1}{4}\right)^{1/4}, \tag{3}$$

where a is the orbital semi-major axis given in the same units as $R_\star$. We obtained a value of 947 ± 28 K, which indicates that TOI-5398 b is unlikely to be affected by the hot-Jupiter anomalous radius inflation mechanism (Thorngren et al. 2016). By contrast, the $T_{\rm eq}$ of the hot-Saturn TOI-2000 c is slightly above 1000 K (Sha et al. 2023); therefore, considering the $T_{\rm eq} = 1000$ K threshold and the fact that its orbital period exceeds 10 days, we describe TOI-5398 b as a warm-Saturn planet.

In addition, TOI-5398 b is located in the Neptunian 'savanna' (Bourrier et al. 2023), a light deficit of planets close to the hot-Neptune desert (Lecavelier Des Etangs 2007; Mazeh et al. 2016).

The sub-Neptune TOI-5398 c is one of the very few inner companions to short-period gas giants with precise values of both mass and radius. In fact, only four small planets with $R_{\rm p} < 4\ R_\oplus$ in compact systems ($P \lesssim 15$ d) have mass measurements: WASP-47 d, WASP-47 e (Vanderburg et al. 2017), TOI-1130 c (Korth et al. 2023), and TOI-2000 b. It is worth noting that they have quite different bulk densities (see Fig. 17), ranging from being composed of rocky cores to having masses and radii similar to those of Neptune and Uranus. The latter composition is true for TOI-5398 c, which shares a bulk density similar to that of the inner companion planet WASP-47 d. As a result, we provide additional evidence that inner companions to transiting giant planets tend to have the same density diversity as other small planets (Sha et al. 2023).

5.3. Ephemeris improvements

An important step of our analysis is the derivation of new and updated mean ephemeris for TOI-5398 b and c. Our best-fit

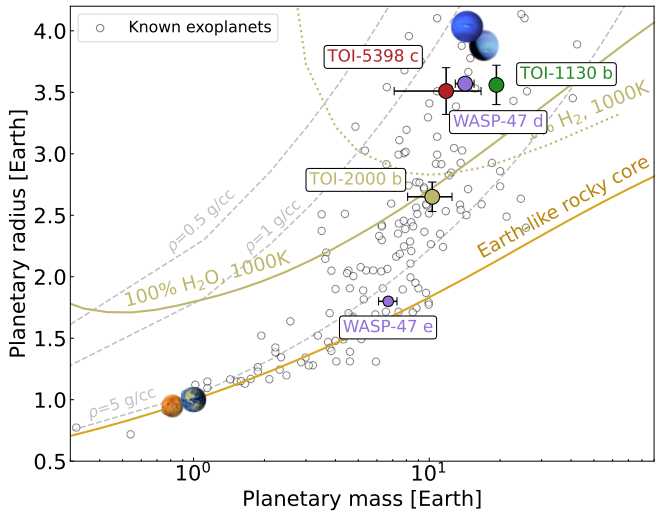

Fig. 17. Mass–radius distribution of all confirmed planets with $R_p < 4\,R_\oplus$ from the NASA Exoplanet Archive with mass and radius determination better than 20%. The red dot represents TOI-5398 c, the beige dot TOI-2000 b, the green dot TOI-1130 c, and the violet dots are respectively WASP-47 d and e. We include the Solar System planets Earth, Venus, Uranus, and Neptune. We add theoretical mass–radius curves from Zeng et al. (2019): solid brown indicates an Earth-like rocky core (32.5% Fe and 67.5% MgSiO3), beige a 100% water world at 1000 K, and dotted beige a 1% hydrogen envelope and 99% Earth-like rocky core at the same temperature. Grey dashed curves represent densities $\rho = 0.5$, 1, and 5 g cm^{-3}, respectively.

relation for the warm Saturn and the sub-Neptune are:

$$T_{0,\mathrm{b}} = 2459616.49232 \pm 0.00022\,\mathrm{BJD_{TDB}} + N \times (10.590547 \pm 0.000012), \quad (4)$$

$$T_{0,\mathrm{c}} = 2459628.6178 \pm 0.0009\,\mathrm{BJD_{TDB}} + N \times (4.77271 \pm 0.00016), \quad (5)$$

where the variable N is an integer number commonly referred to as the 'epoch' and arbitrarily set to zero at our reference transit time T_{ref}. We emphasise that if we propagate the new ephemeris at 2030 January 1 (see Figs. 18 and 19), the level of uncertainty is significantly reduced to ~5 min compared to the previous ~197 min for TOI-5398 b when only TESS photometry was available. This means that when the ground-based photometry is also taken into account, the error bar for TOI-5398 b is 98% smaller than when using TESS data alone. For TOI-5398 c, the error bar is 60% smaller than when we rely solely on TESS data. Accurately identifying the transit windows is crucial for upcoming space-based observations, given the significant investment in observing time and the time-critical nature of such observations. It is crucial to note that no further observations of TOI-5398 are planned in the current TESS Extended Mission[12].

5.4. Planetary system formation and evolution

The obliquity between the planetary orbital plane and the stellar rotation axis is a key diagnostic for the mechanisms of formation and orbital migration of exoplanets (e.g. Naoz et al. 2011). This can be detected with in-transit RVs through the Rossiter-McLaughlin effect (RM, Ohta et al. 2005; Rossiter 1924; McLaughlin 1924; Queloz et al. 2000). Short-period giant planets are thought to form in situ close to the final orbit, or in the outer regions and migrate inward (Dawson & Johnson 2018). Different mechanisms, such as dynamical interactions (high-eccentricity migration) through planet–planet scattering (Marzari et al. 2006) or the Kozai mechanism (Wu & Murray 2003), and disc–planet interaction (Lin et al. 1996), can shrink their orbits. These mechanisms are expected to imprint different signatures in the obliquity of the planets. Scattering encounters should randomise the alignments of the orbital planes, while migration through disc–planet interactions should keep the planetary orbits roughly co-planar throughout the entire process.

The uncommon architecture and moderately young age of TOI-5398 make it particularly promising for measuring the obliquity between the orbital plane of the giant and the spin axis of the star. First, we can access the original configuration when observing systems young enough to have avoided tidal alterations of the obliquity. Then, unlike ordinary short-period giants, we can rule out the high-eccentricity migration scenario (Mustill et al. 2015) for compact systems such as TOI-5398 and test the other formation models through detailed atmospheric characterisation.

Following Eq. (40) from Winn (2010), we determined the expected amplitude of the RV variation produced by the RM effect when planet b transits (58 m s^{-1}) or when planet c transits (7.0 m s^{-1}). Given the activity level of our target (typical RV dispersion: 27 m s^{-1}) and considering a planetary transit timescale,

[12] As it results from the Web TESS Viewing Tool https://heasarc.gsfc.nasa.gov/cgi-bin/tess/webtess/wtv.py

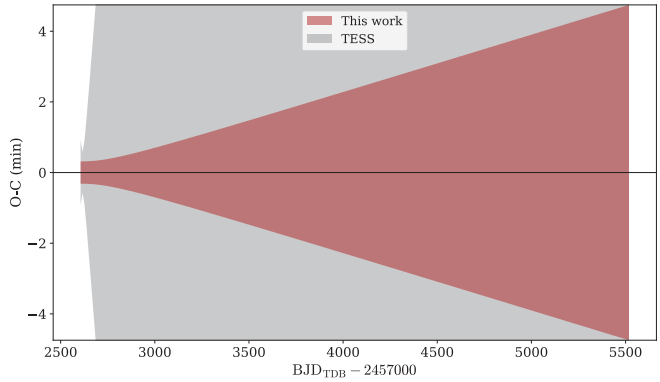

Fig. 18. Ephemeris uncertainty of TOI-5398 b propagated until the start of 2030. On the x-axis, we show the date, while on the y-axis the error bars are in minutes. In grey, we show the uncertainty propagation considering TESS data alone. In red, we show the improvement considering also ground-based photometry data.

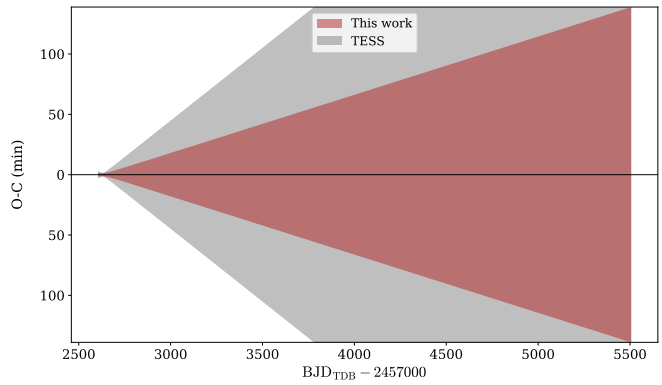

Fig. 19. As in Fig. 18, but for TOI-5398 c.

Table 8. Atmospheric mass-loss simulations.

Core radius	Current age		Evaporation	$t = 5$ Gyr			
($R_\oplus$)	f_{atm}(%)	Mass loss rate (g s^{-1})	time scale[(a)]	Mass ($M_\oplus$)	Radius ($R_\oplus$)	f_{atm}(%)	Mass loss rate (g s^{-1})
			Planet b				
2.4	98.9	5.3×10^{11}	>5 Gyr	56.7	8.9	98.8	1.6×1.6^{10}
5	50.4	5.3×10^{11}	>5 Gyr	56.5	9.3	48.5	2.0×1.6^{10}
7	22.7	5.3×10^{11}	>5 Gyr	56.4	9.5	19.6	2.2×1.6^{10}
			Planet c				
1	7.0	3.5×10^{12}	96 Myr	9.7	1.4	0.4	5.2×10^{8}
1.8	3.5	3.5×10^{12}	27 Myr	10.3	1.8	0.0	0.0
2.5	1.5	3.5×10^{12}	8 Myr	10.2	2.5	0.0	0.0

Notes. [(a)]The evaporation time scale is equal to the time required for losing half of the atmospheric mass.

that is, when the activity level is significantly lower than its typical amplitude, we predict a perfectly suitable detection of the RM effect caused by TOI-5398 b and a possible detection for TOI-5398 c.

5.4.1. Circularisation timescale and α parameter

We calculated the circularisation timescale – denoted τ_{circ} – for TOI-5398 b using Eq. (6) from Matsumura et al. (2008). Assuming a circular orbit and a modified tidal quality factor Q of 10^5 (Ogilvie 2014), the calculated value for τ_{circ} is 2.57 ± 0.88 Gyr, which significantly exceeds the age of the system. This suggests that the near-circular orbit of TOI-5398 b may well be primordial, indicating favourable conditions for preserving its close planetary companion.

Following the methodology described in Bonomo et al. (2017), we computed the parameter α, which represents the ratio of the planet's semi-major axis to its Roche limit. Bonomo et al. (2017) concluded that planets with $\alpha > 5$ and circular orbits are unlikely to undergo high-eccentricity migration. With an α value of 5.6, TOI-5398 b falls in the middle α range (4.55–7.44) for short-period giants with close companions. This finding favours the notion that short-period giants with close companions should not be distinguished between hot ($P < 10$ days) and warm ($P > 10$ days) planets, that is, they belong to the same population of exoplanets, distinct in turn from the typical giants that experience the high-eccentricity migration scenario.

5.4.2. Atmospheric mass-loss

We investigated how the planetary masses, radii, and atmospheric mass-loss rates change with time due to photoevaporation and internal heating. We evaluated the mass-loss rate of the two planets' atmospheres using the hydro-based approximation developed by Kubyshkina et al. (2018a,b), coupled with the planetary core–envelope model by Lopez & Fortney (2014) and the MESA Stellar Tracks (MIST; Choi et al. 2016). For the stellar X-ray emission at different ages, we adopted the analytic description by Penz et al. (2008), with the current X-ray luminosity of $L_x = 10^{29}$ erg s^{-1} in the 5–100 Å band. This value was derived from the rotation-activity relationships by Pizzolato et al. (2003), and closely resembles the median X-ray luminosity of Hyades stars. The stellar EUV luminosity (100–920 Å) was computed at any given time using the scaling law by Sanz-Forcada et al. (2022). The subsequent paragraphs present the outcomes of our forward-in-time simulations, which include the evolution of the extreme-ultraviolet (XUV) irradiation and the planetary structure in response to stellar behaviour. More details on our modelling of atmospheric evaporation are provided in Maggio et al. (2022) and Damasso et al. (2023).

We performed several simulations assuming different possible values for the planetary core radius at the current age. The test cases were selected by comparing them with the grids of planetary internal structures by Fortney et al. (2007), assuming cores composed of 50% rocks and 50% ices. For planet b, we explored core radii ranging from 2.4 to 7 $R_\oplus$, corresponding to core masses of 10 to 25 $M_\oplus$. Regarding planet c, due to its smaller size, we limited our analysis to core radii between 1 and 2.5 $R_\oplus$, with core masses of ~10 $M_\oplus$. Table 8 shows the results of the simulations.

In our reference model for planet b, the core has a radius of $R_{core} = 5\ R_\oplus$ and a core mass of $M_{core} \sim 29 M_\oplus$, resulting in an atmospheric mass fraction f_{env} of ~50%. The current photo-evaporation rate is $\sim 5.3 \times 10^{11}$ g s^{-1}, and the planet will maintain a large envelope mass fraction throughout its main sequence lifetime, with $f_{env} \sim 48\% M_p$ at time $t \sim 5$ Gyr. Its radius will only be reduced by ~10 %. In the range explored, these results depend little on the assumed characteristics of the core.

Conversely, the evolution of the inner planet is very different due to the smaller distance from the host star, higher equilibrium temperature, and higher high-energy irradiation. Our reference model has a core radius of $R_{core} = 1.8\ R_\oplus$ and a core mass of $M_{core} \sim 10\ M_\oplus$, resulting in an atmospheric mass fraction f_{env} of $\sim 3.5\% M_p$. The current photo-evaporation rate is $\sim 3.5 \times 10^{12}$ g s^{-1}, and the planet will lose its entire envelope in $\lesssim$200 Myr from now. The planetary size will decrease to match that of the core. However, a larger core radius implies a smaller atmospheric mass fraction and shorter evaporation timescales. For example, for a core radius $R_{core} = 1\ R_\oplus$, the planet would keep a residual atmospheric envelope even at $t = 5$ Gyr.

5.4.3. Global formation history of TOI-5398

The different masses of the two planets could be either primordial or, as suggested by their different evaporation rates as discussed in Sect. 5.4.2, the result of distinct photoevaporation histories. However, these two scenarios have different implications regarding formation regions and bulk compositions. Our

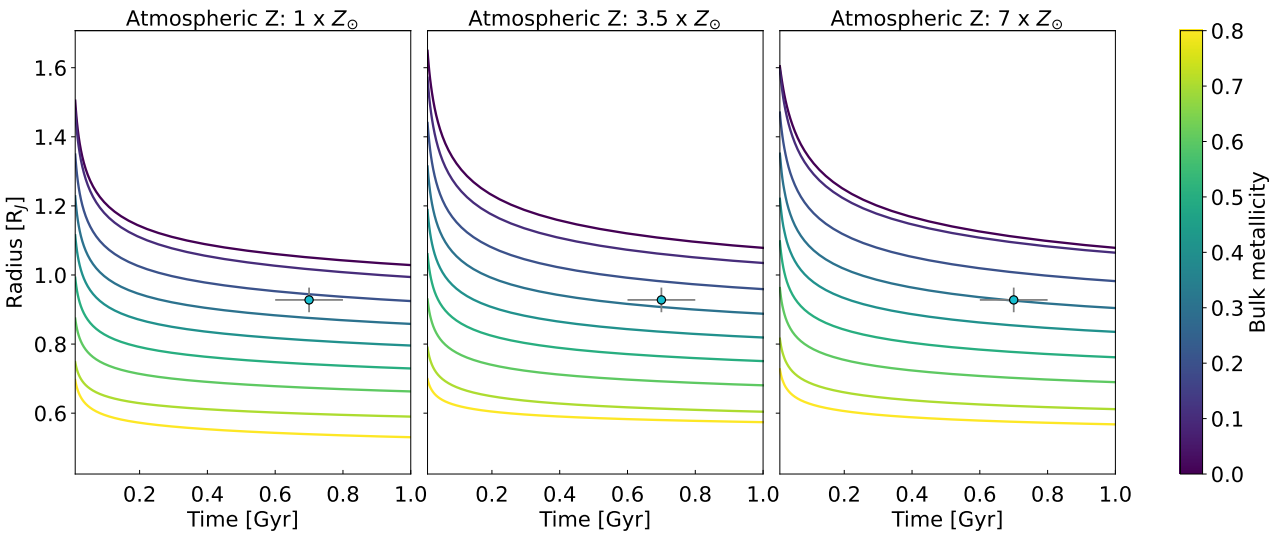

Fig. 20. Radius evolution in time (x-axis) for various bulk metallicities (coloured lines, in units of planet b masses). The three plots adopt three different atmospheric heavy-element mass fractions. The light-blue dot represents TOI-5398 b.

preliminary exploration of the formation tracks of the two planets using the methodology from Johansen et al. (2019) highlights the following possibilities.

For the mass of TOI-5398 c to be primordial or close to the original one, the planet should not have captured significant quantities of disc gas after reaching its pebble isolation mass. This condition is satisfied if the planet had started its formation beyond about 10 au and comparatively late (~1 Myr) in the life of its native disc. However, in this scenario, TOI-5398 b should still be able to capture its present gaseous envelope. For this to occur, planet b should have started its formation at an earlier time (~0.1 Myr) than planet c: as a result, planet b would already be close to its current orbit while planet c is forming and migrating, and the two planets would have to cross orbits to reach their current architecture. Such an encounter would likely result in a planet–planet scattering event; this scenario would result in higher eccentricities and inclinations than the currently observed ones. Even in the case where the dynamical excitation created by the planet–planet scattering event is removed by the interactions of the two planets with the disc gas, the density of planet c appears too low for a realistic mixture of rock and ice resulting from its growth track (as a comparison, the density of the ice-rich dwarf planet Pluto is 2 g cm^{-3}).

The other possible scenario results from the two planets having started forming early in the lifetime of their native disc at a few astronomical units from their host star. In this case, the simulated growth tracks favour a scenario where planet c possessed an extended primordial atmosphere of comparable mass to that of planet b. In this scenario, the present-day mass disparity between the two planets would result from their different photoevaporation histories, with planet c experiencing a much higher mass loss than its outer counterpart. Their gas-accretion phases would have occurred close to their final orbits, in the innermost and hottest regions of the native disc, which suggests that their atmospheres could exhibit stellar composition.

5.5. Planetary bulk composition prediction

Accurate data on mass, eccentricity, and radius allow us to measure precise inner bulk densities and to explore the differences in planetary structure and evolution, from inflated hot Jupiters (HJs) to 'over-dense' warm Jupiters (WJs; Fortney et al. 2021). While the prediction of hotter interiors and larger radii for HJs (Guillot et al. 1996) compared to Jupiter has been proven correct, identifying the mechanism(s) behind the anomalously large radii of some HJs remains a challenge (Thorngren & Fortney 2018). For non-inflated giant planets ($F_\star < 2 \times 10^8$ erg s^{-1} cm^{-2}), Thorngren et al. (2016) found a relation between planet mass and bulk metallicity, which confirms a key prediction of the core-accretion planet formation model (Mordasini et al. 2014). A recent study (Müller & Helled 2023b) presents the current knowledge of mass–metallicity trends for warm giant exoplanets (Teske et al. 2019; Müller et al. 2020; Müller & Helled 2023a), and raises some doubts about its extent and existence. Müller & Helled (2023b) link this ambiguity to theoretical uncertainties on the assumed models and the need for accurate stellar age and atmospheric measurements.

Understanding this relationship and answering the open questions regarding giants require the characterisation of planets and host stars, focusing on the metal enrichment of planetary atmospheres (Miller & Fortney 2011). This is particularly true for warm giants – which are scarce among confirmed planets[13] – unaffected by the radius inflation mechanism, as we can reasonably constrain their bulk metal enrichment and interpret atmospheric features more safely (Thorngren et al. 2016).

TOI-5398 b is a perfect case study if we consider both its low insolation $F_\star$ and its robust age estimation. Therefore, we estimated its planetary bulk heavy-element mass fraction (or bulk metallicity) using evolution models[14] from Müller & Helled (2021). Figure 20 shows the radius evolution for various bulk metallicities (coloured lines) for three different atmospheric heavy-element mass fractions. The bulk heavy-element mass fraction of TOI-5398 b varies between 20 and 30 per cent of its total mass, depending on the adopted atmospheric metallicity. Our result follows the mass–metallicity trend from Thorngren et al. (2016), but the heavy-element mass appears to be slightly lower than expected. Therefore, we may infer that the trend from Müller & Helled (2023a), which predicts a lower heavy-element

[13] Only 20 warm giants have precise bulk densities (density determination better than 20%) in the NASA Exoplanet Archive.
[14] https://github.com/tiny-hippo/planetsynth/blob/main

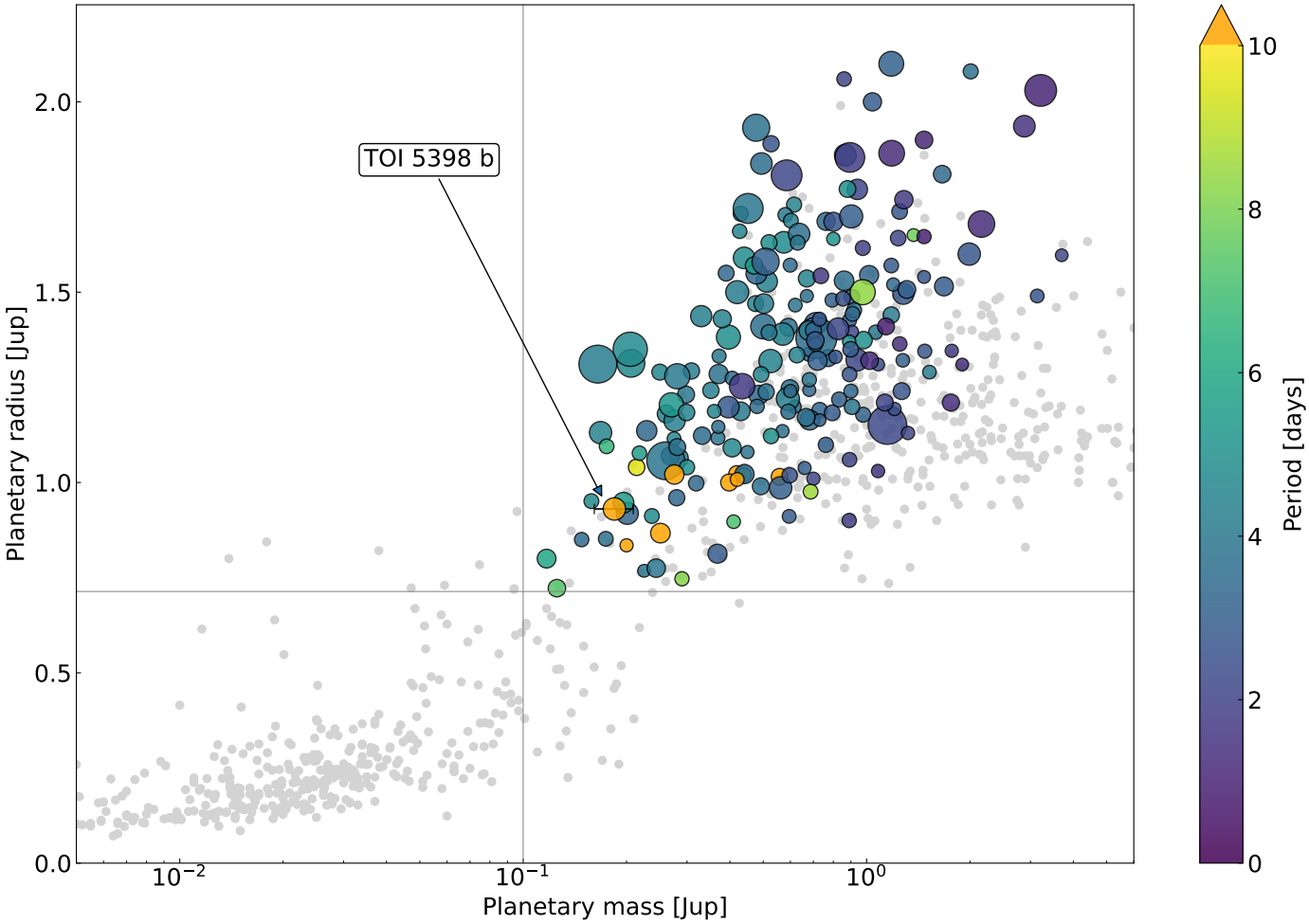

Fig. 21. Mass–radius distribution of all the confirmed planets present in the TEPCat catalogue (Southworth 2011). The orbital period of a planet is colour-coded when it has TSM > 90, $M_p > 0.1\ M_J$, and $R_p > 8\ R_\oplus$. Planets without these characteristics are coloured grey. The dot size tracks the TSM. The planetary mass is shown on a logarithmic scale.

mass for a given planetary mass compared to Thorngren et al. (2016), might offer a more plausible explanation of our result.

5.6. Future atmospheric characterisation

To break the degeneracy in determining the planetary bulk composition, it is crucial to perform atmospheric measurements and to get information on metal enrichment. Müller & Helled (2023b) show that atmospheric measurements by JWST and Ariel can significantly reduce this degeneracy and that this is particularly promising for warm giant planets (Müller & Helled 2023a). A precise characterisation of the TOI-5398 b atmosphere will be crucial in order to validate or disprove formation and evolution theories.

TOI-5398 is a fascinating compact system, as planet b has the highest transmission spectroscopy metric (TSM, Kempton et al. 2018) value (~300) among warm giant planets ($10 < P < 100$, $M_p > 0.1\ M_J$) currently known, making it ideal for atmospheric characterisation by JWST. Indeed, the TSM parameter quantifies the expected signal-to-noise ratio in transmission spectroscopy for a given planet, and according to Kempton et al. (2018), the atmosphere of a giant planet is considered amenable to JWST observations when its TSM value is greater than 90. In Fig. 21, we include all confirmed planets, with colour-coding only for those with a TSM > 90, and $M_p > 0.1\ M_J$. In this plot, we show the planetary masses versus radii, where planets are colour-coded according to their orbital period. We colour-code planets with periods longer than 10 days in orange to highlight the warm-giant planets, which are defined as giant planets with periods exceeding 10 days (e.g. Yee et al. 2021; Gan et al. 2023 and references therein). Instead, the size of the dots tracks the TSM. For comparison, WASP-47 b has only a modest TSM value of ~47 (Bryant & Bayliss 2022).

5.7. Characterisation with JWST/NIRSpec

TOI-5398 b is an ideal candidate for precise transmission spectroscopy and atmospheric characterisation, with a focus on the carbon-to-oxygen (C/O) ratio. This ratio is essential for understanding planetary formation mechanisms and grasping planetary atmosphere composition, shedding light on volatile content and atmospheric chemistry. The availability of carbon and oxygen determines different chemical reactions as well as the stability of molecules of planetary atmospheres. Understanding the C/O ratio helps in predicting the composition and behaviour of atmospheric constituents like carbon dioxide (CO2), carbon monoxide (CO), methane (CH4), and water (H2O; Keyte et al. 2023).

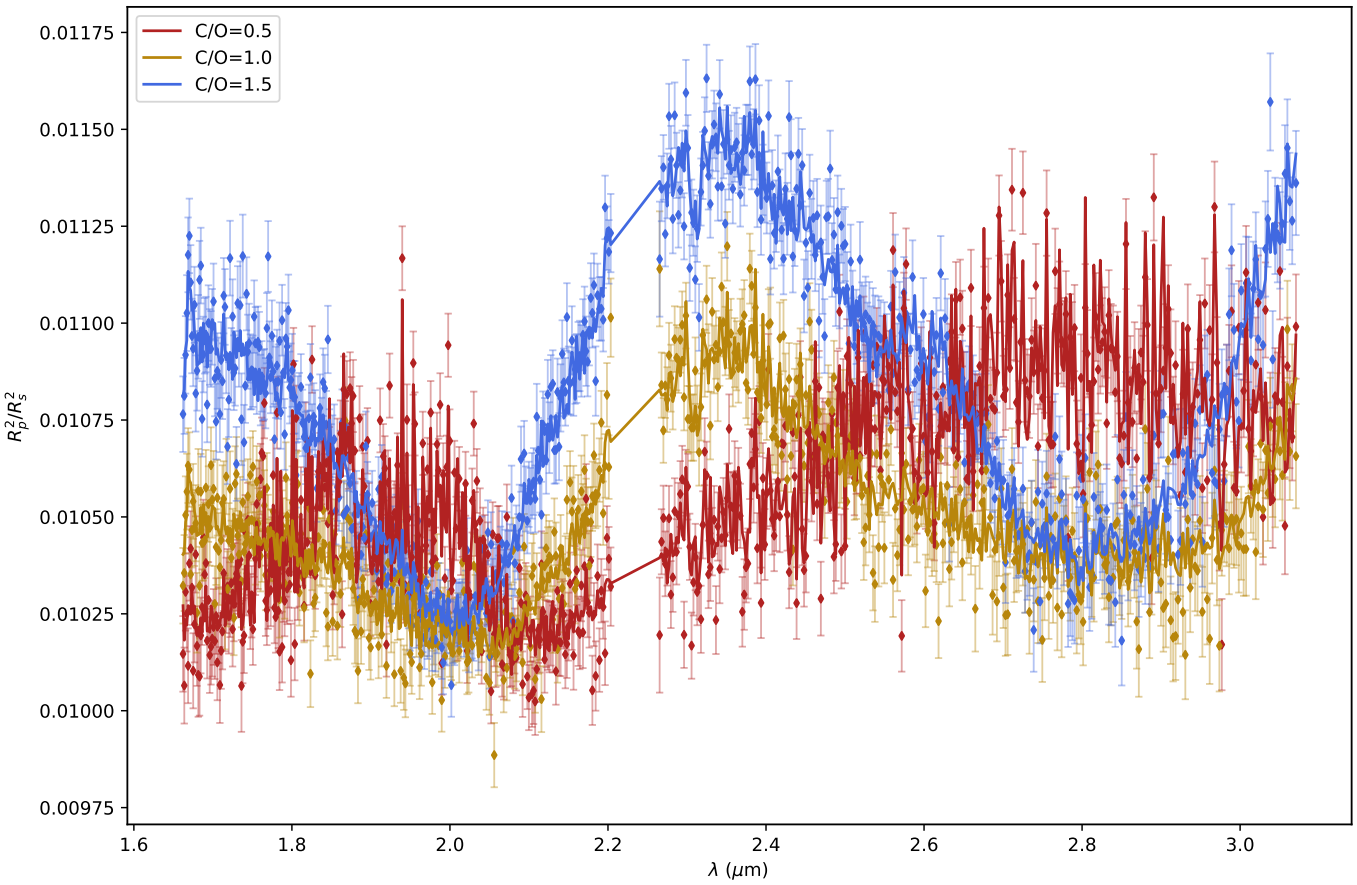

Fig. 22. NIRSpec observation simulation using the g235h disperser with f170lp filter (scatter points) and best-fit models from TauREx (lines). The three colours indicate three scenarios: C/O = 0.5 in red, C/O = 1.0 in yellow, and C/O = 1.5 in blue.

To test the feasibility of atmospheric characterisation using JWST, we investigated three different atmospheric scenarios for TOI-5398 b. We assumed equilibrium chemistry as a function of temperature and pressure using FastChem (Stock et al. 2018) and three different C/O ratios: 0.5, 1.0, and 1.5. We used FastChem within TauREx3 (Al-Refaie et al. 2021) using the `taurex-fastchem`[15] plugin. TauREx is a retrieval code that uses a Bayesian approach to infer atmospheric properties from observed data, utilising a forward model to generate synthetic spectra by solving the radiative transfer equation throughout the atmosphere. We used all the possible gases contributions within FastChem and the active absorption contribution given by K, Na, HCN, H2CO, CH4, CO, CO2, C2H2, C2H4, H2O, NH3, SiO, TiO, VO, and SO2 opacities.

After generating the transmission spectra using TauREX+FastChem, we simulated a JWST observation using Pandexo (Batalha et al. 2017), a software tool specifically developed for the JWST mission. The software allows users to model and simulate various atmospheric scenarios, incorporating factors such as atmospheric composition, temperature profiles, and molecular opacities. We simulated a NIRSpec observation in bots mode using the s1600a1 aperture with g235h disperser, sub2048 subarray, nrsrapid read mode, and f170lp filter. We simulated one single transit and an observation of 1.75 T_{14} in length to ensure robust baseline coverage. We fixed this instrumental configuration for all three scenarios. In Fig. 22, we show the resulting spectra for the different C/O ratios and their best-fit models.

We performed three atmospheric retrievals on the NIRSpec/JWST simulations using a Nested Sampling algorithm with the `nestle`[16] library with 1000 live points. We used the `cuda` transmission model with the `taurex-cuda`[17] TauREx plugin. We fitted three parameters: the radius of the planet R_p, the equilibrium temperature of the atmosphere $T_{\rm eq}$, and the C/O ratios.

Using NIRspec with the g235h disperser wavelength range (1.66–3.07 µm), we can assess the C/O ratio under the three assumptions (see Table 9). In particular, when assuming C/O ratios of 0.5 and 1.0, we can retrieve the correct value within a 1σ error bar, while under the C/O = 1.5 assumption, we retrieved a value of 1.87 ± 0.15, within a 2.5σ error bar.

The three atmospheres can be explained with three distinct sets of parameters (Fig. 23). The results of atmospheric retrievals confirm and quantify the feasibility of atmospheric characterisation using NIRSpec@JWST. Furthermore, they demonstrate that TOI-5398 b is an excellent candidate for comprehensive atmospheric analysis, to measure the C/O ratio, and therefore to constrain planet formation theories for this system.

[15] https://pypi.org/project/taurex-fastchem

[16] https://github.com/kbarbary/nestle

[17] https://github.com/ucl-exoplanets/taurex-cuda_public

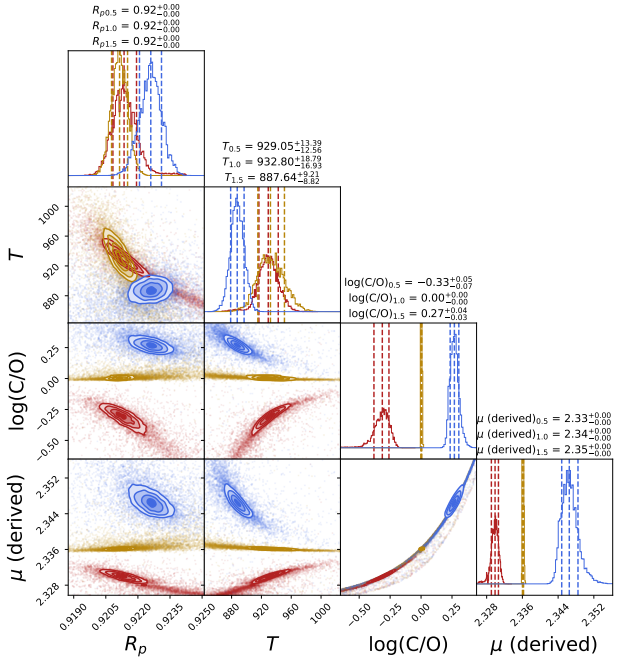

Fig. 23. Posterior distributions for the three different scenarios. We show C/O = 0.5 in red, C/O = 1.0 in yellow, and C/O = 1.5 in blue.

Table 9. Retrieval results for the three different scenarios.

Parameter	C/O = 0.5	C/O = 1.0	C/O = 1.5
R_p (R_J)	$0.9214^{+0.0006}_{-0.0005}$	0.9211 ± 0.0004	0.9226 ± 0.0005
$T_{\rm eq}$ (K)	929 ± 13	932^{+19}_{-17}	887 ± 9
C/O	$0.47^{+0.06}_{-0.07}$	$1.005^{+0.009}_{-0.008}$	1.87 ± 0.15
μ (derived)	2.3298 ± 0.0008	2.3361 ± 0.0001	2.3467 ± 0.0019

6. Conclusions

In this study, we present the discovery of the youngest transiting planetary system containing a sub-Neptune planet orbiting interior to a Saturn-mass planet with $P < 15$ days. Using HARPS-N RV measurements of the host star TOI-5398 and multi-dimensional GPs, we modelled the stellar activity and confirmed the planetary nature of both candidates identified in the TESS light curve measuring their masses. Furthermore, our methodology allows us to accurately determine the stellar parameters.

With a TSM value of around 300, the warm Saturn TOI-5398 b is the most suitable warm giant planet for atmospheric characterisation using JWST. Such investigations are crucial in order to validate or disprove existing formation and evolution theories. By measuring atmospheric chemistry, we can gain information on metal enrichment and effectively break the degeneracy in determining the planetary bulk composition.

The presence of two planets in this relatively young system offers the opportunity to examine distinct evolutionary paths over the first hundreds of millions of years following system formation, under the influence of the same host star. In this study, we provide a characterisation of the system, with a special focus on the future evolution of the planetary atmospheres. Future works will focus on investigating the past evolution of the system. We explored the evolution of the atmospheres of both planets, considering the decay of stellar activity and XUV irradiation with time. We estimated that given reasonable assumptions regarding core radius and mass, planet b probably retains a substantial atmosphere, with a mass fraction of $\sim 0.5 M_{\rm p}$, making it amenable to investigation with transmission spectroscopy. Conversely, planet c is expected to possess a tiny atmospheric envelope. At the current age, the mass-loss rate of planet c exceeds that of planet b by a factor of 7, implying that planet c will completely lose its residual atmosphere within a few hundred million years, while planet b will retain a thick atmosphere even at the solar age.

Notably, TESS observed TOI-5398 during Sector 48 and no further observations are planned in the current Extended Mission. Consequently, our ground-based light curves play a pivotal role in refining the ephemeris of both planets. The improved ephemeris values calculated here are vital for future follow-up observations and surveys, including those conducted by CHEOPS, JWST, and upcoming missions such as PLATO and Ariel, along with telescopes such as the ELT.

Acknowledgements. We are extremely grateful to the anonymous referee for their meticulous feedback, which undoubtedly improved the quality of this manuscript. Based on observations collected at *Copernico* 1.82 m telescope (Asiago Mount Ekar, Italy) INAF – Osservatorio Astronomico di Padova. This work has made use of data from the European Space Agency (ESA) mission *Gaia* (https://www.cosmos.esa.int/gaia), processed by the *Gaia* Data Processing and Analysis Consortium (DPAC, https://www.cosmos.esa.int/web/gaia/dpac/consortium). Funding for the DPAC has been provided by national institutions, in particular, the institutions participating in the *Gaia* Multilateral Agreement. This article is based on observations made with the MuSCAT2 instrument, developed by ABC, at Telescopio Carlos Sánchez operated on the island of Tenerife by the IAC in the Spanish Observatorio del Teide. This work has been supported by the PRIN-INAF 2019 "Planetary systems at young ages (PLATEA)". This work is partly financed by the Spanish Ministry of Economics and Competitiveness through grants PGC2018-098153-B-C31. This work is partly supported by JSPS KAKENHI Grant Numbers JP17H04574, JP18H01265, and JP18H05439, Grant-in-Aid for JSPS Fellows Grant Number JP20J21872, JST PRESTO Grant Number JPMJPR1775, and a University Research Support Grant from the National Astronomical Observatory of Japan (NAOJ). This work makes use of observations from the LCOGT network. Part of the LCOGT telescope time was granted by NOIRLab through the Mid-Scale Innovations Program (MSIP). MSIP is funded by NSF. This research has made use of the Exoplanet Follow-up Observation Program (ExoFOP; DOI: 10.26134/ExoFOP5) website, which is operated by the California Institute of Technology, under contract with the National Aeronautics and Space Administration under the Exoplanet Exploration Program. Funding for the TESS mission is provided by NASA's Science Mission Directorate. K.A.C. and C.N.W. acknowledge support from the TESS mission via subaward s3449 from MIT. T.Zi. acknowledges NVIDIA Academic Hardware Grant Program for the use of the Titan V GPU card. This work is partly supported by JST CREST Grant Number JPMJCR1761. The postdoctoral fellowship of K.B. is funded by F.R.S.-FNRS grant T.0109.20 and by the Francqui Foundation. D.V.C. and I.A.S. acknowledge the support of M.V. Lomonosov Moscow State University Program of Development. R.L. acknowledges funding from University of La Laguna through the Margarita Salas Fellowship from the Spanish Ministry of Universities ref. UNI/551/2021-May 26, and under the EU Next Generation funds. This work is partly supported by the CHEOPS ASI-INAF agreement n. 2019-29-HH.0. G.N. thanks for the research funding from the Ministry of Education and Science programme the "Excellence Initiative – Research University" conducted at the Centre of Excellence in Astrophysics and Astrochemistry of the Nicolaus Copernicus University in Toruń, Poland. We acknowledge the use of public TESS data from pipelines at the TESS Science Office and at the TESS Science Processing Operations Center. Resources supporting this work were provided by the NASA High-End Computing (HEC) Program through the NASA Advanced Supercomputing (NAS) Division at Ames Research Center for the production of the SPOC data products. A.M., D.L., D.T., and D.P. acknowledge partial financial support from the ARIEL ASI-INAF agreement n.2021-5-HH.0. A.M. also acknowledges "The HOT-ATMOS Project" (PRIN-INAF 2019). D.P. acknowledges the support from the Istituto Nazionale di Oceanografia e Geofisica Sperimentale (OGS) and CINECA through the program "HPC-TRES (High Performance Computing Training and Research for Earth Sciences)" award number 2022-05. P.K. acknowledges the funding from a grant LTT-20015.

References

Agol, E., Steffen, J., Sari, R., & Clarkson, W. 2005, MNRAS, 359, 567
Al-Refaie, A. F., Changeat, Q., Waldmann, I. P., & Tinetti, G. 2021, ApJ, 917, 37
Baliunas, S. L., Donahue, R. A., Soon, W. H., et al. 1995, ApJ, 438, 269
Baraffe, I., Homeier, D., Allard, F., & Chabrier, G. 2015, A&A, 577, A42
Baratella, M., D'Orazi, V., Biazzo, K., et al. 2020a, A&A, 640, A123
Baratella, M., D'Orazi, V., Carraro, G., et al. 2020b, A&A, 634, A34
Barragán, O., Aigrain, S., Rajpaul, V. M., & Zicher, N. 2022, MNRAS, 509, 866
Barragán, O., Gillen, E., Aigrain, S., et al. 2023, MNRAS, 522, 3458
Batalha, N. E., Mandell, A., Pontoppidan, K., et al. 2017, PASP, 129, 064501
Becker, J. C., Vanderburg, A., Adams, F. C., Rappaport, S. A., & Schwengeler, H. M. 2015, ApJ, 812, L18
Benatti, S., Nardiello, D., Malavolta, L., et al. 2019, A&A, 630, A81
Biazzo, K., D'Orazi, V., Desidera, S., et al. 2022, A&A, 664, A161
Bonomo, A. S., Desidera, S., Benatti, S., et al. 2017, A&A, 602, A107
Bonomo, A. S., Zeng, L., Damasso, M., et al. 2019, Nat. Astron., 3, 416
Borsato, L., Marzari, F., Nascimbeni, V., et al. 2014, A&A, 571, A38
Borsato, L., Malavolta, L., Piotto, G., et al. 2019, MNRAS, 484, 3233
Borsato, L., Piotto, G., Gandolfi, D., et al. 2021, MNRAS, 506, 3810
Borucki, W. J., Koch, D., Basri, G., et al. 2010, Science, 327, 977
Bouma, L. G., Hartman, J. D., Brahm, R., et al. 2020, AJ, 160, 239
Bourrier, V., Dumusque, X., Dorn, C., et al. 2018, A&A, 619, A1
Bourrier, V., Attia, O., Mallonn, M., et al. 2023, A&A, 669, A63
Brown, T. M., Baliber, N., Bianco, F. B., et al. 2013, PASP, 125, 1031
Bryant, E. M., & Bayliss, D. 2022, AJ, 163, 197
Buchhave, L. A., Bakos, G. Á., Hartman, J. D., et al. 2010, ApJ, 720, 1118
Buchhave, L. A., Latham, D., Johansen, A., et al. 2012, Nature, 486, 375
Butler, R. P., Marcy, G. W., Williams, E., Hauser, H., & Shirts, P. 1997, ApJ, 474, L115
Cañas, C. I., Wang, S., Mahadevan, S., et al. 2019, ApJ, 870, L17
Capitanio, L., Lallement, R., Vergely, J. L., Elyajouri, M., & Monreal-Ibero, A. 2017, A&A, 606, A65
Carlberg, J. K., Cunha, K., Smith, V. V., & Majewski, S. R. 2012, ApJ, 757, 109
Carleo, I., Malavolta, L., Lanza, A. F., et al. 2020, A&A, 638, A5
Carleo, I., Desidera, S., Nardiello, D., et al. 2021, A&A, 645, A71
Casagrande, L., Portinari, L., & Flynn, C. 2006, MNRAS, 373, 13
Casagrande, L., Lin, J., Rains, A. D., et al. 2021, MNRAS, 507, 2684
Castelli, F., & Kurucz, R. L. 2003, in Modelling of Stellar Atmospheres, 210, eds. N. Piskunov, W. W. Weiss, & D. F. Gray, A20
Choi, J., Dotter, A., Conroy, C., et al. 2016, ApJ, 823, 102
Collier Cameron, A., Mortier, A., Phillips, D., et al. 2019, MNRAS, 487, 1082
Collier Cameron, A., Ford, E. B., Shahaf, S., et al. 2021, MNRAS, 505, 1699
Collins, K. 2019, in American Astronomical Society Meeting Abstracts, 233, 140.05
Cosentino, R., Lovis, C., Pepe, F., et al. 2012, SPIE Conf. Ser., 8446, 84461V
Covino, E., Esposito, M., Barbieri, M., et al. 2013, A&A, 554, A28
Cowan, N. B., & Agol, E. 2011, ApJ, 729, 54
Cummings, J. D., Deliyannis, C. P., Maderak, R. M., & Steinhauer, A. 2017, AJ, 153, 128
Cutri, R. M., Skrutskie, M. F., van Dyk, S., et al. 2003, VizieR Online Data Catalog, II/246
Damasso, M., Lanza, A. F., Benatti, S., et al. 2020, A&A, 642, A133
Damasso, M., Locci, D., Benatti, S., et al. 2023, A&A, 672, A126
da Silva, L., Girardi, L., Pasquini, L., et al. 2006, A&A, 458, 609
Dawson, R. I., & Johnson, J. A. 2018, ARA&A, 56, 175
Desidera, S., Covino, E., Messina, S., et al. 2015, A&A, 573, A126
Desidera, S., Damasso, M., Gratton, R., et al. 2023, A&A, 675, A158
D'Orazi, V., Oliva, E., Bragaglia, A., et al. 2020, A&A, 633, A38
Doyle, A. P., Davies, G. R., Smalley, B., Chaplin, W. J., & Elsworth, Y. 2014, MNRAS, 444, 3592
Dragomir, D., Teske, J., Günther, M. N., et al. 2019, ApJ, 875, L7
Dutra-Ferreira, L., Pasquini, L., Smiljanic, R., Porto de Mello, G. F., & Steffen, M. 2016, A&A, 585, A75
Eastman, J., Siverd, R., & Gaudi, B. S. 2010, PASP, 122, 935
Eastman, J., Gaudi, B. S., & Agol, E. 2013, PASP, 125, 83
Faria, J. P., Santos, N. C., Figueira, P., & Brewer, B. J. 2018, J. Open Source Softw., 3, 487
Fűrész, G. 2008, PhD thesis, University of Szeged, Hungary
Foreman-Mackey, D., Hogg, D. W., Lang, D., & Goodman, J. 2013, PASP, 125, 306
Fortney, J. J., Marley, M. S., & Barnes, J. W. 2007, ApJ, 659, 1661
Fortney, J. J., Dawson, R. I., & Komacek, T. D. 2021, J. Geophys. Res. (Planets), 126, e06629
Gaia Collaboration (Prusti, T., et al.) 2016, A&A, 595, A1
Gaia Collaboration (Vallenari, A., et al.) 2023, A&A, 674, A1
Gan, T., Wang, S. X., Wang, S., et al. 2023, AJ, 165, 17
Gelman, A., & Rubin, D. B. 1992, Stat. Sci., 7, 457
Gomes da Silva, J., Santos, N. C., Bonfils, X., et al. 2011, A&A, 534, A30
Gomes da Silva, J., Santos, N. C., Boisse, I., Dumusque, X., & Lovis, C. 2014, A&A, 566, A66
Gomes da Silva, J., Figueira, P., Santos, N., & Faria, J. 2018, J. Open Source Softw., 3, 667
Gomes da Silva, J., Santos, N. C., Adibekyan, V., et al. 2021, A&A, 646, A77
Goodman, J., & Weare, J. 2010, Commun. Appl. Math. Comput. Sci., 5, 65
Grouffal, S., Santerne, A., Bourrier, V., et al. 2022, A&A, 668, A172
Grunblatt, S. K., Howard, A. W., & Haywood, R. D. 2015, ApJ, 808, 127
Guillot, T., Burrows, A., Hubbard, W. B., Lunine, J. I., & Saumon, D. 1996, ApJ, 459, L35
Haywood, R. D., Collier Cameron, A., Queloz, D., et al. 2014, MNRAS, 443, 2517
Hellier, C., Anderson, D. R., Collier Cameron, A., et al. 2012, MNRAS, 426, 739
Høg, E., Fabricius, C., Makarov, V. V., et al. 2000, A&A, 355, L27
Holman, M. J., & Murray, N. W. 2005, Science, 307, 1288
Hord, B. J., Colón, K. D., Berger, T. A., et al. 2022, AJ, 164, 13
Howell, S. B., Sobeck, C., Haas, M., et al. 2014, PASP, 126, 398
Huang, C., Wu, Y., & Triaud, A. H. M. J. 2016, ApJ, 825, 98
Huang, C. X., Quinn, S. N., Vanderburg, A., et al. 2020a, ApJ, 892, L7
Huang, C. X., Vanderburg, A., Pál, A., et al. 2020b, RNAAS, 4, 204
Hunter, A., Macgregor, A., Szabo, T., Wellington, C., & Bellgard, M. 2012, Source Code for Biology and Medicine, 7
Husser, T. O., Wende-von Berg, S., Dreizler, S., et al. 2013, A&A, 553, A6
Jenkins, J. M. 2002, ApJ, 575, 493
Jenkins, J. M., Chandrasekaran, H., McCauliff, S. D., et al. 2010, SPIE Conf. Ser., 7740, 77400D
Jenkins, J. M., Twicken, J. D., McCauliff, S., et al. 2016, SPIE Conf. Ser., 9913, 99133E
Jenkins, J. M., Tenenbaum, P., Seader, S., et al. 2020, Kepler Data Processing Handbook: Transiting Planet Search, Kepler Science Document KSCI-19081-003, 9
Jensen, E. 2013, Astrophysics Source Code Library [record ascl:1306.007]
Johansen, A., Ida, S., & Brasser, R. 2019, A&A, 622, A202
John, A. A., Collier Cameron, A., & Wilson, T. G. 2022, MNRAS, 515, 3975
John, A. A., Collier Cameron, A., Faria, J. P., et al. 2023, MNRAS, 525, 1687
Johnson, D. R. H., & Soderblom, D. R. 1987, AJ, 93, 864
Kass, R. E., & Raftery, A. E. 1995, J. Am. Stat. Assoc., 90, 773
Kempton, E. M. R., Bean, J. L., Louie, D. R., et al. 2018, PASP, 130, 114401
Keyte, L., Kama, M., Booth, A. S., et al. 2023, Nat. Astron., 7, 684
Kipping, D. M. 2013, MNRAS, 435, 2152
Knutson, H. A., Fulton, B. J., Montet, B. T., et al. 2014, ApJ, 785, 126
Kochanek, C. S., Shappee, B. J., Stanek, K. Z., et al. 2017, PASP, 129, 104502
Korth, J., Gandolfi, D., Šubjak, J., et al. 2023, A&A, 675, A115
Kostov, V. B., Schlieder, J. E., Barclay, T., et al. 2019, AJ, 158, 32
Kovács, G., Zucker, S., & Mazeh, T. 2002, A&A, 391, 369
Kreidberg, L. 2015, PASP, 127, 1161
Kubyshkina, D., Fossati, L., Erkaev, N. V., et al. 2018a, ApJ, 866, L18
Kubyshkina, D., Fossati, L., Erkaev, N. V., et al. 2018b, A&A, 619, A151
Kurucz, R. L. 1992, in The Stellar Populations of Galaxies, 149, eds. B. Barbuy, & A. Renzini, 225
Lacedelli, G., Malavolta, L., Borsato, L., et al. 2021, MNRAS, 501, 4148
Lallement, R., Vergely, J. L., Valette, B., et al. 2014, A&A, 561, A91
Lanza, A. F., Bonomo, A. S., Moutou, C., et al. 2010, A&A, 520, A53
Latham, D. W., Rowe, J. F., Quinn, S. N., et al. 2011, ApJ, 732, L24
Lecavelier Des Etangs, A. 2007, A&A, 461, 1185
Li, J., Tenenbaum, P., Twicken, J. D., et al. 2019, PASP, 131, 024506
Lin, D. N. C., Bodenheimer, P., & Richardson, D. C. 1996, Nature, 380, 606
Lind, K., Asplund, M., & Barklem, P. S. 2009, A&A, 503, 541
Lissauer, J. J., Marcy, G. W., Rowe, J. F., et al. 2012, ApJ, 750, 112
Lopez, E. D., & Fortney, J. J. 2014, ApJ, 792, 1
Lovis, C., Dumusque, X., Santos, N. C., et al. 2011, ArXiv e-prints [arXiv:1107.5325]
Maggio, A., Locci, D., Pillitteri, I., et al. 2022, ApJ, 925, 172
Malavolta, L., Nascimbeni, V., Piotto, G., et al. 2016, A&A, 588, A118
Malavolta, L., Lovis, C., Pepe, F., Sneden, C., & Udry, S. 2017, MNRAS, 469, 3965
Malavolta, L., Mayo, A. W., Louden, T., et al. 2018, AJ, 155, 107
Maldonado, J., Martínez-Arnáiz, R. M., Eiroa, C., Montes, D., & Montesinos, B. 2010, A&A, 521, A12
Mamajek, E. E., & Hillenbrand, L. A. 2008, ApJ, 687, 1264
Mancini, L., Esposito, M., Covino, E., et al. 2022, A&A, 664, A162
Mann, A. W., Johnson, M. C., Vanderburg, A., et al. 2020, AJ, 160, 179
Mantovan, G., Montalto, M., Piotto, G., et al. 2022, MNRAS, 516, 4432
Mardling, R. A., & Lin, D. N. C. 2002, ApJ, 573, 829
Martin, D. C., Fanson, J., Schiminovich, D., et al. 2005, ApJ, 619, L1
Marzari, F., Scholl, H., & Tricarico, P. 2006, A&A, 453, 341
Matsumura, S., Takeda, G., & Rasio, F. A. 2008, ApJ, 686, L29

Mazeh, T., Holczer, T., & Faigler, S. 2016, A&A, 589, A75
McCully, C., Volgenau, N. H., Harbeck, D.-R., et al. 2018, SPIE Conf. Ser., 10707, 107070K
McLaughlin, D. B. 1924, ApJ, 60, 22
Messina, S., Nardiello, D., Desidera, S., et al. 2022, A&A, 657, A3
Miller, N., & Fortney, J. J. 2011, ApJ, 736, L29
Montalto, M., Piotto, G., Marrese, P. M., et al. 2021, A&A, 653, A98
Montes, D., López-Santiago, J., Gálvez, M. C., et al. 2001, MNRAS, 328, 45
Mordasini, C., Klahr, H., Alibert, Y., Miller, N., & Henning, T. 2014, A&A, 566, A141
Morris, R. L., Twicken, J. D., Smith, J. C., et al. 2020, Kepler Data Processing Handbook: Photometric Analysis, Kepler Science Document KSCI-19081-003, 6, ed. J. M. Jenkins.
Morton, T. D. 2012, ApJ, 761, 6
Morton, T. D. 2015, Astrophysics Source Code Library [record ascl:1503.010]
Morton, T. D., Giacalone, S., & Bryson, S. 2023, RNAAS, 7, 107
Müller, S., & Helled, R. 2021, MNRAS, 507, 2094
Müller, S. & Helled, R. 2023a, A&A, 669, A24
Müller, S., & Helled, R. 2023b, Front. Astron. Space Sci., 10, 1179000
Müller, S., Ben-Yami, M., & Helled, R. 2020, ApJ, 903, 147
Mustill, A. J., Davies, M. B., & Johansen, A. 2015, ApJ, 808, 14
Naoz, S., Farr, W. M., Lithwick, Y., Rasio, F. A., & Teyssandier, J. 2011, Nature, 473, 187
Naponiello, L., Mancini, L., Damasso, M., et al. 2022, A&A, 667, A8
Nardiello, D. 2020, MNRAS, 498, 5972
Nardiello, D., Piotto, G., Deleuil, M., et al. 2020, MNRAS, 495, 4924
Nardiello, D., Malavolta, L., Desidera, S., et al. 2022, A&A, 664, A163
Narita, N., Fukui, A., Kusakabe, N., et al. 2019, J. Astron. Telescopes Instrum. Syst., 5, 015001
Nascimbeni, V., Piotto, G., Bedin, L. R., & Damasso, M. 2011, A&A, 527, A85
Nascimbeni, V., Cunial, A., Murabito, S., et al. 2013, A&A, 549, A30
Nascimbeni, V., Borsato, L., Zingales, T., et al. 2023, A&A, 673, A42
Nesvorný, D., Kipping, D., Terrell, D., et al. 2013, ApJ, 777, 3
Newton, E. R., Mann, A. W., Tofflemire, B. M., et al. 2019, ApJ, 880, L17
Ogilvie, G. I. 2014, ARA&A, 52, 171
Ohta, Y., Taruya, A., & Suto, Y. 2005, ApJ, 622, 1118
Parviainen, H. 2015, MNRAS, 450, 3233
Parviainen, H., & Aigrain, S. 2015, MNRAS, 453, 3821
Parviainen, H., Tingley, B., Deeg, H. J., et al. 2019, A&A, 630, A89
Penz, T., Micela, G., & Lammer, H. 2008, A&A, 477, 309
Pepe, F., Mayor, M., Galland, F., et al. 2002, A&A, 388, 632
Pizzolato, N., Maggio, A., Micela, G., Sciortino, S., & Ventura, P. 2003, A&A, 397, 147
Queloz, D., Eggenberger, A., Mayor, M., et al. 2000, A&A, 359, A13
Rajpaul, V., Aigrain, S., Osborne, M. A., Reece, S., & Roberts, S. 2015, MNRAS, 452, 2269
Rasmussen, C. E., Williams, C. K., et al. 2006, Gaussian Processes for Machine Learning, 1 (Springer)
Ricker, G. R., Winn, J. N., Vanderspek, R., et al. 2015, J. Astron. Telescopes Instrum. Syst., 1, 014003
Robertson, P., Endl, M., Cochran, W. D., & Dodson-Robinson, S. E. 2013, ApJ, 764, 3
Rossiter, R. A. 1924, ApJ, 60, 15
Sanz-Forcada, J., López-Puertas, M., Nortmann, L., & Lampón, M. 2022, 21st Cambridge Workshop on Cool Stars, Stellar Systems, and the Sun, https://backoffice.inviteo.com/upload/compte153/Base/inscriptions_projets/fichier/108345-posterjsanzcs21.pdf
Schlaufman, K. C., & Winn, J. N. 2016, ApJ, 825, 62
Schlegel, D. J., Finkbeiner, D. P., & Davis, M. 1998, ApJ, 500, 525
Schwarz, G. 1978, Ann. Stat., 6, 461
Sestito, P., & Randich, S. 2005, A&A, 442, 615
Sha, L., Vanderburg, A. M., Huang, C. X., et al. 2023, MNRAS, 524, 1113
Shappee, B. J., Prieto, J. L., Grupe, D., et al. 2014, ApJ, 788, 48
Smith, J. C., Stumpe, M. C., Van Cleve, J. E., et al. 2012, PASP, 124, 1000
Sneden, C. 1973, ApJ, 184, 839
Southworth, J. 2011, MNRAS, 417, 2166
Stassun, K. G., & Torres, G. 2016, AJ, 152, 180
Stassun, K. G., & Torres, G. 2021, ApJ, 907, L33
Stassun, K. G., Collins, K. A., & Gaudi, B. S. 2017, AJ, 153, 136
Stassun, K. G., Corsaro, E., Pepper, J. A., & Gaudi, B. S. 2018, AJ, 155, 22
Stassun, K. G., Oelkers, R. J., Paegert, M., et al. 2019, AJ, 158, 138
Stock, J. W., Kitzmann, D., Patzer, A. B. C., & Sedlmayr, E. 2018, MNRAS, 479, 865
Storn, R., & Price, K. 1997, J. Global Optim., 11, 341
Strakhov, I. A., Safonov, B. S., & Cheryasov, D. V. 2023, Astrophys. Bull., 78, 235
Stumpe, M. C., Smith, J. C., Van Cleve, J. E., et al. 2012, PASP, 124, 985
Stumpe, M. C., Smith, J. C., Catanzarite, J. H., et al. 2014, PASP, 126, 100
Terquem, C., & Papaloizou, J. C. B. 2007, ApJ, 654, 1110
Teske, J. K., Thorngren, D., Fortney, J. J., Hinkel, N., & Brewer, J. M. 2019, AJ, 158, 239
Thorngren, D. P., & Fortney, J. J. 2018, AJ, 155, 214
Thorngren, D. P., Fortney, J. J., Murray-Clay, R. A., & Lopez, E. D. 2016, ApJ, 831, 64
Torres, G., Andersen, J., & Giménez, A. 2010, A&ARv, 18, 67
Trifonov, T., Brahm, R., Jordán, A., et al. 2023, AJ, 165, 179
Tuson, A., Queloz, D., Osborn, H. P., et al. 2023, MNRAS, 523, 3090
Twicken, J. D., Clarke, B. D., Bryson, S. T., et al. 2010, SPIE Conf. Ser., 7740, 774023
Twicken, J. D., Catanzarite, J. H., Clarke, B. D., et al. 2018, PASP, 130, 064502
Vanderburg, A., Becker, J. C., Buchhave, L. A., et al. 2017, AJ, 154, 237
Van Eylen, V., Albrecht, S., Huang, X., et al. 2019, AJ, 157, 61
Weiss, L. M., Marcy, G. W., Rowe, J. F., et al. 2013, ApJ, 768, 14
Winn, J. N. 2010, arXiv e-prints [arXiv:1001.2010]
Wolfgang, A., Rogers, L. A., & Ford, E. B. 2016, ApJ, 825, 19
Wright, E. L., Eisenhardt, P. R. M., Mainzer, A. K., et al. 2010, AJ, 140, 1868
Wu, Y., & Murray, N. 2003, ApJ, 589, 605
Yee, S. W., Winn, J. N., & Hartman, J. D. 2021, AJ, 162, 240
Yee, S. W., Winn, J. N., Hartman, J. D., et al. 2022, AJ, 164, 70
Zechmeister, M., & Kürster, M. 2009, A&A, 496, 577
Zeng, L., Jacobsen, S. B., Sasselov, D. D., et al. 2019, PNAS, 116, 9723
Zhu, W., Dai, F., & Masuda, K. 2018, RNAAS, 2, 160

[1] Dipartimento di Fisica e Astronomia "Galileo Galilei", Università di Padova, Vicolo dell'Osservatorio 3, 35122 Padova, Italy
e-mail: giacomo.mantovan@phd.unipd.it
[2] INAF – Osservatorio Astronomico di Padova, Vicolo dell'Osservatorio 5, 35122 Padova, Italy
[3] INAF – Osservatorio Astronomico di Palermo, Piazza del Parlamento 1, 90134 Palermo, Italy
[4] INAF – Osservatorio Astronomico di Trieste, Via Giambattista Tiepolo, 11, 34131 Trieste (TS), Italy
[5] INAF – Osservatorio Astrofisico di Torino, via Osservatorio 20, 10025 Pino Torinese, Italy
[6] Leibniz-Institut für Astrophysik Potsdam (AIP), An der Sternwarte 16, 14482 Potsdam, Germany
[7] INAF – Osservatorio Astronomico di Roma, Via Frascati 33, 00078 Monte Porzio Catone (Roma), Italy
[8] Department of Physics and Astronomy, Vanderbilt University, Nashville, TN 37235, USA
[9] Department of Physics, Fisk University, Nashville, TN 37208, USA
[10] SUPA, School of Physics & Astronomy, University of St Andrews, North Haugh, St Andrews KY169SS, UK; Centre for Exoplanet Science, University of St Andrews, North Haugh, St Andrews KY169SS, UK
[11] Center for Astrophysics | Harvard & Smithsonian, 60 Garden Street, Cambridge, MA 02138, USA
[12] Space Science and Astrobiology Division, NASA Ames Research Center, MS 245-3, Moffett Field, CA 94035, USA
[13] SETI Institute, Mountain View, CA 94043 USA/NASA Ames Research Center, Moffett Field, CA 94035, USA
[14] NASA Ames Research Center, Moffett Field, CA 94035, USA
[15] INAF – Osservatorio Astrofisico di Catania, Oss. Astr. Catania, via S. Sofia 78, 95123 Catania, Italy
[16] Department of Astrophysical Sciences, Princeton University, Princeton, NJ 08544, USA
[17] ESO, Karl-Schwarzschild-str. 2, 85748 Garching, Germany
[18] Sternberg Astronomical Institute Lomonosov Moscow State University, Moscow, Russia
[19] Instituto de Astrofísica de Canarias (IAC), 38205 La Laguna, Tenerife, Spain
[20] Departamento de Astrofísica, Universidad de La Laguna (ULL), Avd. Astrofísico Francisco Sánchez s/n, 38206 La Laguna, Tenerife, Spain
[21] Astrobiology Research Unit, Université de Liège, 19C Allée du 6 Août, 4000 Liège, Belgium
[22] Department of Earth, Atmospheric and Planetary Science, Massachusetts Institute of Technology, 77 Massachusetts Avenue, Cambridge, MA 02139, USA

[23] Acton Sky Portal (private observatory), Acton, MA, USA
[24] INAF – Osservatorio Astronomico di Brera, Via E. Bianchi 46, 23807 Merate (LC), Italy
[25] McDonald Observatory and Center for Planetary Systems Habitability; The University of Texas, Austin Texas, USA
[26] Center for Computational Astrophysics, Flatiron Institute, 162 Fifth Avenue, New York, NY 10010, USA
[27] Department of Physics and Kavli Institute for Astrophysics and Space Research, Massachusetts Institute of Technology, Cambridge, MA 02139, USA
[28] Fundación Galileo Galilei – INAF, Rambla José Ana Fernandez Pérez 7, 38712 Breña Baja, TF, Spain
[29] Astronomical Institute, Czech Academy of Sciences, Fričova 298, 251 65, Ondřejov, Czech Republic
[30] Department of Astronomy & Astrophysics, University of Chicago, Chicago, IL 60637, USA
[31] Department of Astronomy, Wellesley College, Wellesley, MA 02481, USA
[32] Komaba Institute for Science, The University of Tokyo, 3-8-1 Komaba, Meguro, Tokyo 153-8902, Japan
[33] Astrobiology Center, 2-21-1 Osawa, Mitaka, Tokyo 181-8588, Japan
[34] Institute of Astronomy, Faculty of Physics, Astronomy and Informatics, Nicolaus Copernicus University, Grudziądzka 5, 87-100 Toruń, Poland
[35] Royal Astronomical Society, Burlington House, Piccadilly, London W1J 0BQ, UK
[36] Department of Aeronautics and Astronautics, MIT, 77 Massachusetts Avenue, Cambridge, MA 02139, USA
[37] Department of Physics, University of Warwick, Gibbet Hill Road, Coventry CV4 7AL, UK
[38] Dipartimento di Matematica e Fisica, Università Roma Tre, Via della Vasca Navale 84, 00146 Roma, Italy
[39] Department of Astronomy, The University of Texas at Austin, Austin, TX 78712, USA
[40] Dipartimento di Fisica, Università degli Studi di Torino, via Pietro Giuria 1, 10125 Torino, Italy

Appendix A: Spectroscopic time series

The spectroscopic time series (RV, BIS, $\log R'_{\rm HK}$, H_α, FWHM, $W_{\rm CCF}$) will be available in electronic format as supplementary material for the paper at the CDS.

Appendix B: Statistical validation

In the first step of our vetting and validation study, we used *Gaia* EDR3 data to identify nearby contaminating stars that might be blended eclipsing binaries (BEBs). This analysis shows that besides TOI-5398, there is a star (*Gaia* DR2 750888586899153536) at 45.3″ separation from TOI-5398 that might reproduce the transit signal of TOI-5398.02; see Fig. B.1. To ensure that the transits of TOI-5398.02 are genuine and not caused by contaminant neighbours, we carried out the in- and out-of-transit difference centroid check outlined by Nardiello et al. (2020) and Nardiello (2020). We show the outcomes in Fig. B.2. The in- and out-of-transit mean difference centroids are consistent with TOI-5398's position and are far from any potential contaminants, further proving the planetary nature of TOI-5398.02.

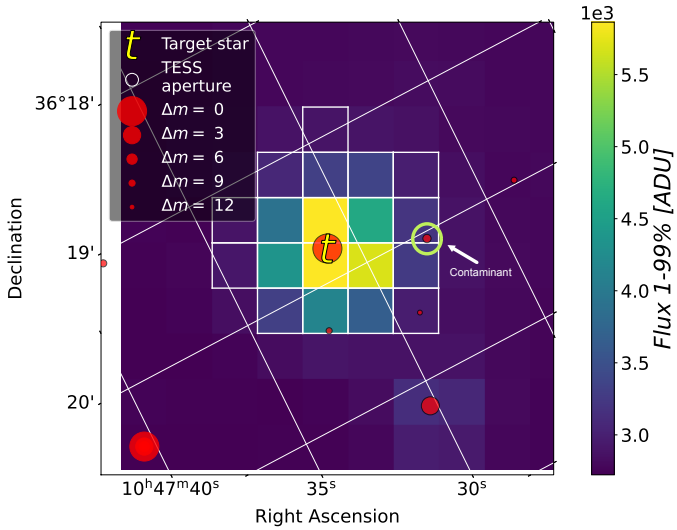

Fig. B.1. *Gaia* stars identified in the TESS field. The letter 't' denotes the position of TOI-5398, while the position of the potential contaminant star is enclosed in a green circle.

To corroborate that TOI-5398.02 is not an FP, we used the VESPA[18] software (Morton 2012, 2015) as a final check. We followed the procedure adopted in Mantovan et al. (2022), which takes into account the major issues reported in Morton et al. (2023) and allows us to get reliable results while using VESPA. We used our detrended light curve (see Sect. 2.1), which we normalised using WOTAN, and we phase-folded after removing TOI-5398 b's signal identified by the SPOC pipeline (see Sect. 4.1.1). We find a 100% probability of having a Keplerian transiting companion around TOI-5398, while the probability of an FP is of the order of ~9 x 10^{-4}. It is important to note that candidates in multi-planet systems have a higher probability of being genuine planets (Latham et al. 2011; Lissauer et al. 2012). Therefore, our FPP (false positive probability) should be even lower. All these analyses show that TOI-5398.02 is completely statistically vetted and only needs to go through reconnaissance

[18] https://github.com/timothydmorton/VESPA

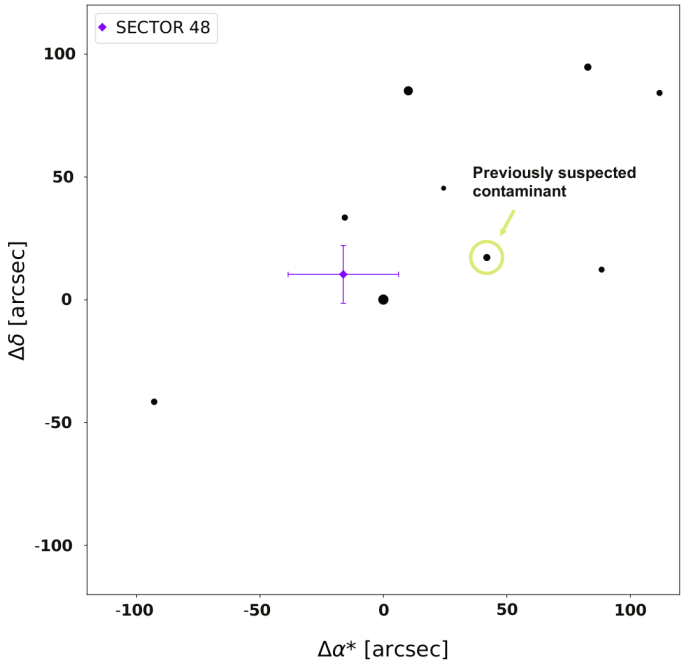

Fig. B.2. Computation of the in- and out-of-transit difference centroid test for Sector 48 (violet dot and error bars). The potential contaminant star's location is instead surrounded by a green circle.

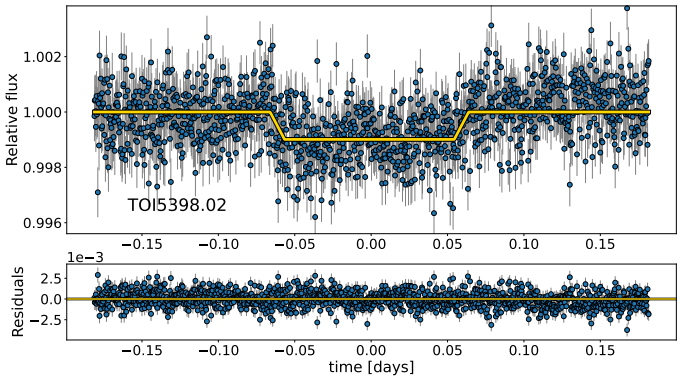

Fig. B.3. SAP-corrected light curve of TOI-5398 c that has been detrended, normalised, and phase-folded. The gold line is a trapezoidal fitting model produced by VESPA.

spectroscopy to be promoted to the status of a statistically validated planetary companion (Mantovan et al. 2022). As a result of the extensive HARPS-N spectroscopy examination of the planetary system TOI-5398, the sub-Neptune exoplanet is statistically validated and will henceforth be labelled TOI-5398 c.

High-angular-resolution observations described in Sect. 2.6 rule out – down to the sensitivity of the data – the presence of a stellar companion that could have been missed by *Gaia* photometry. The detection limits for companions (ΔI_c mag vs separation) were translated into physical properties of companions of the star using the expected V-I colour from the $T_{\rm eff}$ of the target and the stellar models by Baraffe et al. (2015) for the suitable age of the system. The mass detection limits span from 0.65 $M_\odot$ at 13 au (projected separation) to 0.28 $M_\odot$ at 50 au, and 0.17 $M_\odot$ at 100 au.

Appendix C: Independent RV analysis using TWEAKS

The HARPS-N CCFs were independently analysed for planetary signals using TWEAKS (Time and Wavelength domain stEllar Activity mitigation using KIMA and SCALPELS). This pipeline was designed to achieve a sub-m/s detection threshold at extended orbital periods (John et al. 2023). This is achieved by obtaining a set of time-domain stellar activity-decorrelation vectors using SCALPELS (Collier Cameron et al. 2021), by doing principal-component analysis on the autocorrelation function of the CCF. These basis vectors were then used for the spectral line-shape decorrelation (Collier Cameron et al. 2021) in KIMA (Faria et al. 2018), as John et al. (2022) reported that using the SCALPELS basis vectors to de-trend the RVs for line shape variations results in a model that is significantly better than a model that does not take these stellar activity signatures into account.

A model with up to five unidentified Keplerian signals was used in our first blind search of the RVs using the KIMA nested-sampling package (Faria et al. 2018). As found by John et al. (2022), some planet-like signals elude SCALPELS analysis, and so any remaining rotationally modulated signals were modelled with GP regression applied to the RVs using a quasi-periodic GP kernel. The joint posteriors showed clear detection of planet b at an orbital period of 10.5905 ± 0.0002 days with an RV semi-amplitude of 14.51 ± 3.74 ms^{-1}. Additionally, the GP strongly constrained the stellar rotation to $P_{rot} = 7.36^{+0.11}_{-0.08}$ days. This independent analysis aligns with the RV reference model solution and the stellar parameters discussed in Sect. 3.5.

Appendix D: Combined analysis of HARPS-N, TRES, and McDonald datasets

D.1. Observations and data reduction of TRES data

Spectra of TOI-5398 were obtained between UT 2022 March 28 and 2022 April 19 using the Tillinghast Reflector Echelle Spectrograph (TRES; Fűrész 2008) mounted on the 1.5m Tillinghast Reflector telescope at the Fred Lawrence Whipple Observatory (FLWO) atop Mount Hopkins, Arizona. TRES is an optical, fibre-fed echelle spectrograph with a wavelength range of 390-910nm and a resolving power of R 44 000. The TRES spectra were extracted as described in Buchhave et al. (2010). The spectra were visually inspected to check that there were no additional stellar companions contaminating the RVs. A multi-order relative velocity analysis was then performed by cross-correlating the strongest signal-to-noise observed spectrum as a template, order by order, against the remaining spectra to produce an orbit.

D.2. Modelling of HARPS-N, TRES, and McDonald RVs

We conducted a modelling analysis using `PyORBIT` on the HARPS-N, TRES, and McDonald data using the same configuration and priors as described in Sect. 4.3 (Case 3). The results of this modelling are reported in Table D.1, Fig. D.1, and D.2. Due to the considerable errors associated (see their associated jitters) with these measurements and the less precise activity indexes, the TRES and McDonald RVs were not used in determining the planet parameters, as we could not reliably determine their GP parameters (see their V_c, V_r coefficients and error bars). Consequently, we decided to exclude them from the analysis conducted in our study.

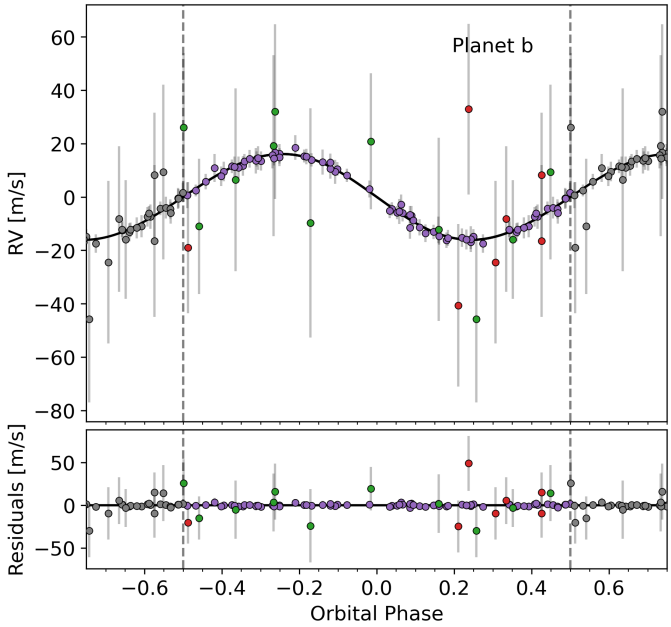

Fig. D.1. Phase-folded RV fit of TOI-5398 b planetary signal. The three different colours represent HARPS-N (violet), TRES (green), and McDonald 2.7m (red) data. The reported error bars include the jitter term, added in quadrature. The bottom panel displays the residuals of the fit.

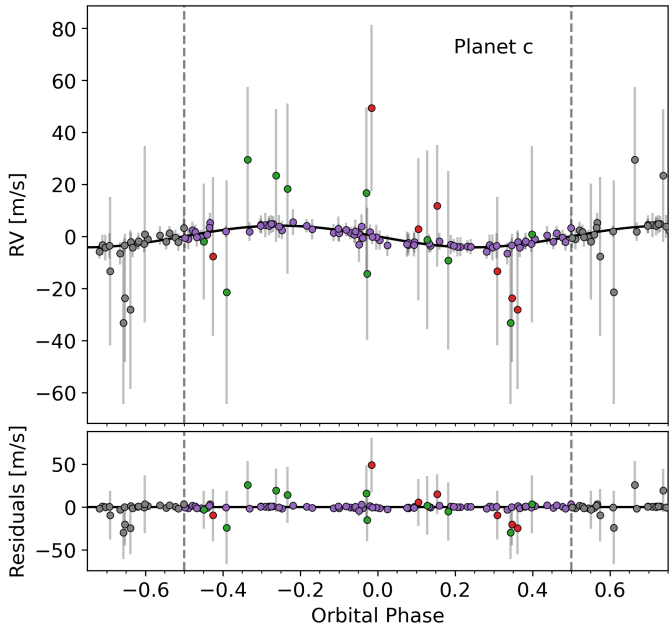

Fig. D.2. As in Fig. D.1, but for planet c.

D.3. Stellar parameters using TRES spectra

The TRES spectra were also used to derive stellar parameters using the Stellar Parameter Classification tool (SPC; Buchhave et al. 2012). SPC cross correlates an observed spectrum against a grid of synthetic spectra based on the Kurucz atmospheric model (Kurucz 1992), which derives the effective temperature T_{eff} = 5933 ± 50 K, surface gravity $\log g$ = 4.42 ± 0.10, metallicity $[m/H]$ = 0.03 ± 0.08, and rotational velocity of the star $v \sin i_\star$ = 8.4 ± 0.5 km s^{-1}. The stellar parameters align with the estimates that we presented in Sect. 3 and Table 2.

Table D.1. Priors and outcomes of the model of planet b and c from the analysis of combined HARPS-N, TRES, and McDonald spectroscopic series.

GP framework parameters			
Parameter	Unit	Prior	Value
Uncorrelated RV jitter HARPS-N ($\sigma^{\rm RV}_{\rm jitter,0}$)	m s^{-1}	...	$1.28^{+1.4}_{-0.89}$
RV offset HARPS-N ($\gamma^{\rm RV}_0$)	m s^{-1}	...	$-9435.1^{+3.7}_{-3.9}$
Uncorrelated RV jitter McDonald ($\sigma^{\rm RV}_{\rm jitter,0}$)	m s^{-1}	...	26^{+29}_{-18}
RV offset McDonald ($\gamma^{\rm RV}_0$)	m s^{-1}	...	27778 ± 20
Uncorrelated RV jitter TRES ($\sigma^{\rm RV}_{\rm jitter,0}$)	m s^{-1}	...	$11.3^{+13}_{-7.8}$
RV offset TRES ($\gamma^{\rm RV}_0$)	m s^{-1}	...	-6^{+23}_{-20}
Uncorrelated BIS jitter ($\sigma^{\rm BIS}_{\rm jitter,0}$)	m s^{-1}	...	$17.3^{+1.8}_{-1.6}$
BIS offset ($\gamma^{\rm BIS}_0$)	m s^{-1}	...	$10.9^{+3.1}_{-3.0}$
Uncorrelated log R'_{HK} jitter ($\sigma^{\rm logR'_{HK}}_{\rm jitter,0}$)		...	$0.0132^{+0.0015}_{-0.0014}$
log R'_{HK} offset ($\gamma^{\rm logR'_{HK}}_0$)		...	-4.4165±0.0035
Uncorrelated Hα jitter ($\sigma^{\rm H\alpha}_{\rm jitter,0}$)		...	0.0018±0.0002
Hα offset ($\gamma^{\rm H\alpha}_0$)		...	0.1513±0.0006
Uncorrelated FWHM jitter ($\sigma^{\rm FWHM}_{\rm jitter,0}$)	km s^{-1}	...	0.043±0.004
FWHM offset ($\gamma^{\rm FWHM}_0$)	km s^{-1}	...	11.36±0.01
Uncorrelated $W_{\rm CCF}$ jitter ($\sigma^{W_{\rm CCF}}_{\rm jitter,0}$)	km s^{-1}	...	$0.0014^{+0.0014}_{-0.0009}$
$W_{\rm CCF}$ offset ($\gamma^{W_{\rm CCF}}_0$)	km s^{-1}	...	3.503±0.004
V_c HARPS-N	m s^{-1}	$\mathcal{U}$(-100.0, 100.0)	$-13.4^{+3.1}_{-3.7}$
V_r HARPS-N	m s^{-1}	$\mathcal{U}$(0.0, 100.0)	$31.3^{+6.7}_{-4.6}$
V_c McDonald	m s^{-1}	$\mathcal{U}$(-100.0, 100.0)	2^{+30}_{-31}
V_r McDonald	m s^{-1}	$\mathcal{U}$(0.0, 100.0)	56^{+27}_{-28}
V_c TRES	m s^{-1}	$\mathcal{U}$(-100.0, 100.0)	-13^{+22}_{-24}
V_r TRES	m s^{-1}	$\mathcal{U}$(0.0, 100.0)	18^{+21}_{-12}
B_c	m s^{-1}	$\mathcal{U}$(-100.0, 100.0)	$6.1^{+4.2}_{-3.8}$
B_r	m s^{-1}	$\mathcal{U}$(-100.0, 100.0)	$-40.7^{+6.2}_{-8.0}$
L_c (log R'_{HK})		$\mathcal{U}$(-0.1, 0.1)	-0.012±0.003
$L2_c$ (Hα)		$\mathcal{U}$(-0.1, 0.1)	$-0.0021^{+0.0004}_{-0.0005}$
$L3_c$ (FWHM)	km s^{-1}	$\mathcal{U}$(-0.5, 0.5)	$-0.046^{+0.009}_{-0.011}$
$L4_c$ ($W_{\rm CCF}$)	km s^{-1}	$\mathcal{U}$(-0.02, 0.02)	$-0.015^{+0.002}_{-0.003}$
Stellar activity			
Parameter	Unit	Prior	Value
Rotational period ($P_{\rm rot}$)	days	$\mathcal{N}$(7.18, 0.21)	7.42±0.04
Decay Timescale of activity ($P_{\rm dec}$)	days	$\mathcal{U}$(10.0, 2000.0)	$26.8^{+3.3}_{-3.1}$
Coherence scale (w)		$\mathcal{U}$(0.01, 0.60)	$0.40^{+0.04}_{-0.03}$
Planet b			
Parameter	Unit	Prior	Value
Orbital period ($P_{\rm b}$)	days	$\mathcal{N}$(10.59049, 0.00002)	10.59049±0.00002
Central time of the first transit ($T_{0,\rm b}$)	BTJD	$\mathcal{N}$(2616.4921, 0.0003)	2616.4921±0.0003
Orbital eccentricity ($e_{\rm b}$)		$\mathcal{N}$(0.00, 0.098)	$0.05^{+0.06}_{-0.04}$
Argument of periastron ($\omega_{\rm b}$)	deg	...	79^{+64}_{-105}
Semi-major axis to stellar radius ratio ($a_{\rm b}/R_\star$)		...	19.9±1.2
Orbital semi-major axis ($a_{\rm b}$)	au	...	$0.098^{+0.004}_{-0.004}$
RV semi-amplitude ($K_{\rm b}$)	m s^{-1}	$\mathcal{U}$(0.01, 100.0)	$16.1^{+1.5}_{-1.5}$
Planetary mass ($M_{\rm p,b}$)	$M_\oplus$	...	$58.8^{+7.7}_{-7.3}$

Table D.1. continued.

Planet c			
Parameter	Unit	Prior	Value
Orbital period (P_c)	days	$\mathcal{N}(4.7734, 0.0004)$	4.7734±0.0004
Central time of the first transit ($T_{0,c}$)	BTJD	$\mathcal{N}(2628.6188, 0.0010)$	2628.6188±0.0010
Orbital eccentricity (e_c)		$\mathcal{N}(0.00, 0.098)$	$0.07^{+0.07}_{-0.05}$
Argument of periastron (ω_c)	deg	...	132^{+93}_{-142}
Semi-major axis to stellar radius ratio ($a_c/R_\star$)		...	11.7±0.7
Orbital semi-major axis (a_c)	au	...	$0.058^{+0.002}_{-0.003}$
RV semi-amplitude (K_c)	m s^{-1}	$\mathcal{U}(0.01, 100.0)$	4.2±1.6
Planetary mass ($M_{p,c}$)	$M_\oplus$	...	$11.6^{+4.7}_{-4.6}$